EXPERIMENTAL CHARACTERIZATION AND PHYSICS-BASED MODELING OF OPTICAL PROPERTY TEMPERATURE DEPENDENCIES IN DOPED METAL OXIDES

by
Michael Collins Brupbacher

A dissertation submitted to Johns Hopkins University in conformity with the
requirements for the degree of Doctor of Philosophy

Baltimore, MD
August, 2017

Abstract

The technical significance of doped metal oxides, and in particular oxides of the "poor" metal aluminum and the transition metal zirconium, is apparent in the abundance of literature regarding their synthesis and optical property characterizations. Processing methods for these doped metal oxides have ranged from traditional solid-state techniques to sol-gel chemistries and innovative thermal spray preparations. Despite the breadth of synthesis routes used to make these materials, a commonality of the importance in the materials science paradigm is undoubtedly observed across a wide variety of applications. As modern-day applications continue to expand the uses for these doped metal oxides, the ability to extend the fundamental and phenomenological theories describing optical properties to include the effects of extreme environmental conditions (e.g. high temperatures) will certainly be of increasing importance.

One such emerging application is found in the optical characterization of aluminized solid rocket propellant fires. Deep space exploration often necessitates the use of radioisotope thermoelectric generators to power instrumentation in the absence of sufficient solar irradiance for conventional solar-cell power generation. In the event of a launch accident there is potential for the release of radioactive material through several pathways, and transition metal oxides have been proposed as surrogates to simulate these various release mechanisms. While the appropriate measurement technique is dependent on the fire region of interest, each proposed dopant transition metal ion (e.g., Cr^{3+}) in an alumina host presents the prospect of capturing unique temperature-dependent optical signatures. The spectral locations of the absorption and fluorescence features provide identification of the dopant in the probed physical location, given that the temperature-

dependent spectral location of the features has either been previously measured or accurately modeled at expected fire temperatures ($T \leq 3100$ K).

Thermal barrier coatings involving oxides of zirconium have found a multitude of applications over several critical industries, including both aerospace and industrial power production. In order to achieve lower thermal conductivities than are intrinsic to the zirconias themselves, these materials are typically thermally-sprayed to introduce significant levels of porosity. Additionally, these zirconias often incorporate transition metal dopants (e.g., yttrium) to achieve phase stability in the most extreme environmental conditions. As the definition of "extreme environmental conditions" continues to evolve to higher temperatures ($T \geq 2273$ K) in response to aerospace application demands, the role of dopants will naturally extend to include the capacity to radiate energy into the surroundings. One material subset that has received little attention in this regard are the rare earth zirconates of the form $Ln_2Zr_2O_7$ (where Ln = La, Nd, Sm). Knowledge of temperature-dependent optical properties for these materials will be integral in effectively designing next-generation coating systems for thermal management.

Owing to the importance of optical properties of various doped metal oxides at elevated temperatures for a variety of applications, this dissertation focuses on experimental characterization and physics-based modeling of optical property temperature dependencies for two specific doped-metal-oxide systems: the transition-metal-doped aluminas (i.e. Cr-doped alumina) and the rare earth zirconates (i.e. $Nd_2Zr_2O_7$). While the optical property measurement techniques employed are of the same for both doped-metal-oxide systems, processing methods to produce these materials vary. Transition-metal-doped alumina powders are prepared via sol-gel chemistries,

whereas rare-earth zirconate powders are obtained commercially and are derived from traditional powder-processing techniques. These doped-metal-oxide powders are thermally-sprayed as thick deposits using atmospheric plasma spray, and from these monolithic coatings are obtained which are suitable for CO_2 laser heating. The facility to produce these materials in their desired physical/structural forms and accurately measure their room-temperature optical properties without debilitating spectral interference from impurities is demonstrated. A supercontinuum-laser-based technique for determination of temperature-dependent optical properties and physics-based modeling of these measurements will also be described. Previously-unreported optical phenomena have been observed at high temperatures in both doped-metal-oxide systems using supercontinuum-laser-based spectroscopy. For the transition-metal-doped aluminas, these relate to absorption band splitting due to thermal and optical anisotropy in the host material, as well as fluorescence quenching due to increased phonon interaction at high temperatures. In the case of the rare earth zirconates, these relate to free-carrier absorption due to extrinsic semiconductor behavior at high temperatures in non-equilibrium phases.

Advisors: Dr. James B. Spicer and Dr. Michael E. Thomas

Readers: Dr. James B. Spicer, Dr. Jonah D. Erlebacher

Acknowledgements

First and foremost, I would like to thank my family and friends for their continued support during these past few years. In particular, I would like to thank my mother Chris, father John and sister Katie – without their unconditional love this work certainly would not have been possible. I would also like to thank my grandparents Caroline and Stanley Taylor, Aunt Stacey Taylor and significant other Amanda Clements for their words of encouragement when needed most.

I have had the pleasure of working with many incredible scientists and engineers at both The Johns Hopkins University (JHU) and The Johns Hopkins University Applied Physics Laboratory (JHU APL). For these individuals, the names of all of which are simply too long to list, I am thankful. To Dr. Dajie Zhang, Mark Buchta, and Dr. Dennis Nagle, I thank you for inciting a curiosity in me that I can hardly contain. To my advisor, Dr. James Spicer, and Dr. Michael Thomas, I thank you for pushing me beyond what I believed to be my capability. To Dr. Jonah Erlebacher, Dr. Ian McCue and Bernard Gaskey, I thank you for reminding me of the joy in science at a difficult time in my research. To the U.S. Department of Energy (DOE), JHU APL, JHU, the JHU Department of Materials Science and Engineering (JHU DMSE) and my dissertation committee, including Dr. James Spicer, Dr. Jonah Erlebacher, Dr. Jacob Khurgin, Dr. Kevin Hemker and Dr. Susanna Thon, I thank you for what surely has been the opportunity of a lifetime.

Contents

List of Tables

List of Figures

Chapter 1: Introduction

1. Introduction

The optical behaviors of chromium-doped α-alumina (polycrystalline) and ruby (single crystal) have importance in a variety of applications that require an understanding of the temperature dependence of related properties. The dependence of fluorescence (specifically, photoemission line-width and -shift) on environmental conditions has attracted significant interest owing to its use in applications ranging from calibration of diamond anvil pressure cells [1] to environmental sensing using remote optical techniques [2-3]. As the complexity of the given application has evolved, so has the physical form of the critical optical sensing element. For instance, thermographic paints and fiber-optic thermometers based on the fluorescence intensity lifetime of Cr-doped α-alumina and ruby have been applied for temperature sensing in static environments at elevated temperatures [2], while in-situ residual stress monitoring via photoluminescence piezo-spectroscopy of Cr-doped, thermally-grown-oxides in the bond coat layers has been proposed for health monitoring of turbine blade thermal barrier coating systems during cool-down [3]. Interestingly, the temperature dependencies of the absorption pump bands in Cr-doped α-alumina and ruby (due to electronic transitions in the octahedrally-coordinated Cr^{3+} ion) have been largely unstudied [4] even though they are intimately related to the temperature dependence of fluorescence.

Ruby has been regarded as “Solid State Spectroscopy’s Serendipitous Servant” by Imbusch and Yen [5] for its wide use in studying the physical processes governing observed optical spectra near and below room-temperature. The most detailed records of the temperature dependence of optical absorption [4] and emission [6] in synthetic ruby at temperatures significantly above room temperature were reported in the early 20th century. While such studies would be considered particularly ambitious even at the present day, dopant concentrations in the synthetic ruby crystals used at the time were not reported and the maximum temperatures for reported spectra were lower than those reached in this work (703 K in [4] and 1273 K in [6], up to 1550 K in this work). Furthermore, only optical emission band locations, not spectra, were reported in [6]. Nonetheless, these works represent important milestones in the progress of high-temperature solid-state spectroscopy, and the authors' observations will be qualitatively compared to results obtained in this work.

The temperature dependence of the green U-band ($^4A_2 \rightarrow {}^4T_2$) absorption in Cr-doped α-alumina is of interest to the aerospace nuclear safety community since this electronic transition could potentially be used as a tracer to map elemental distributions in aluminized solid rocket propellant fires. The use of optical remote sensing techniques for detection and tracking of species relies on a comprehensive understanding of temperature dependence for the various electronic transitions on the energy level diagram of octahedrally-coordinated Cr^{3+} [7]. The ability to measure the signatures of the spectral emissions above the thermal background of the propellant fire (≤ 3100 K [8]) is critical to the success of this type of sensing strategy. While the optical properties might not be directly measured at temperatures of interest, lower temperature measurements can be used to parameterize models that describe the temperature dependence of the absorption bands for this particular dopant/host combination. These models can be applied to assess the feasibility of using optical remote sensing for detection and tracking of the spectral absorption/emission bands at higher temperatures.

Traditionally, absorption band temperature dependencies in doped-metal-oxide systems have been studied via transmission measurements on dense samples using broadband, uncollimated illumination sources such as torches [4] and lamps [9] along with conventional heating methods based on furnaces [4] and hot cells [9] which can contribute significant stray light to the measurement depending on the wavelength range of interest. Several scientific and technological advances now enable characterization of absorption band temperature dependencies using diffuse reflectance measurements that could not be realized previously. These advances involve methods for sample preparation and optical instruments that can be used to perform spectroscopic measurements. In terms of materials synthesis, the use of sol-gel methods [10] in conjunction with atmospheric plasma spray (APS) provides a pathway for the rapid production of thick, monolithic, doped-metal-oxides. It is well known that coatings deposited via APS are inherently microporous [11] and this has benefits for laser heating. The microporosity essentially acts to lower thermal stresses induced by temperature gradients in the material. With respect to instrumentation, the use of a supercontinuum laser source for spectroscopic measurements provides a collimated beam that can be accurately directed to the heated zone on the sample. At the same time its spectral breadth (comparable to a broadband lamp source) permits sampling of material optical properties across a broad wavelength range [12]. Supercontinuum-laser diffuse reflectance spectroscopy has been used for stand-off detection of room-temperature materials such as explosives and fertilizers [13]. In Chapter 2, supercontinuum laser diffuse reflectance spectroscopy is extended to high temperatures and applied to monolithic Cr-doped α-alumina.

The power of the two-flux standard Kubelka-Munk (K-M) theory describing diffuse light propagation in highly-scattering media [14] is in the simplicity of the homogeneous differential equation governing radiation transfer, and is manifest in the wide-ranging applicability of the physical model. In the context of this work, the standard K-M theory refers to the original theory along with any modifications that do not disrupt the homogeneity of the differential equation that is used to describe radiation transfer. Historically, the paper and textile industries have used the standard K-M theory to describe the optical properties of their materials, but the theory also has broad applicability to materials developed in the thermal spray community. For example, the standard K-M theory can be used to investigate the use of doped fluorescent layers between thermal barrier coatings (TBCs) and their substrates. These doped fluorescent layers have been proposed for optical remote sensing of temperature at the TBC/substrate interface [15]. This concept relies on propagation of a pump laser through the TBC to the doped fluorescent layer, where a fluorescent signature is generated and back-transmitted through the TBC to a detector. With knowledge of the diffuse reflectance $R(\lambda)$ and transmittance $T(\lambda)$ spectra of a TBC with known thickness, the spectral K-M absorption $K(\lambda)$ and back-scatter $S(\lambda)$ coefficients can be determined [16]. Using just these two wavelength-dependent parameters, the radiant flux of a pump laser at the surface of the doped fluorescent layer or of a corresponding fluorescent signature at the surface of the TBC can be investigated for arbitrary coating thicknesses. Such a construct can be immensely useful for pump laser and dopant selection for a given a TBC material.

However, application of fluorescence thermometry may rely on knowledge of the relationship between measured absorption of the pump laser and fluorescence escaping the highly-scattering, doped layer – collective information which is not frequently gathered even for the most common combinations of dopant/host materials. The ability to extract temperature-dependent quantum efficiency from supercontinuum laser diffuse reflectance measurements with a K-M model that includes fluorescence is the subject of Chapter 3. This is demonstrated using supercontinuum laser diffuse reflectance measurements for monolithic Cr-doped α-alumina.

When zirconia (ZrO_2) is doped with certain rare earth oxides ($REO_{1.5}$) a single-phase rare earth zirconate having the pyrochlore crystal structure may be obtained. This occurs when the radius of the rare earth ion (RE^{3+}) is sufficiently large relative to the radius of the zirconium ion (Zr^{4+}) ($1.46 < {}^{r_{RE^{3+}}}/_{r_{Zr^{4+}}} < 1.80$) [17]. Several trivalent rare earth ions satisfy this criterion including those of La, Nd, and Sm. In addition to the well-known radius-ratio criterion, studies of the phase stability fields for these rare earth zirconate pyrochlores have shown stability over a wide range of temperatures for the stoichiometric line compounds ($RE_2Zr_2O_7$) as well as a narrow range of stability for off-stoichiometry compositions [18]. These studies have also shown interesting trends in the pyrochlore stability fields with decreasing radius of the rare earth ion, both in the thermal and compositional directions on the phase diagrams. With decreasing radius of the rare earth ion ($r_{La^{3+}} > r_{Nd^{3+}} > r_{Sm^{3+}}$) the pyrochlore phase stability fields narrow in the thermal direction and broaden in the compositional direction. Immediately outside of the pyrochlore stability fields at high temperatures, the rare earth zirconates are found to be in the single-phase defect fluorite crystal structure or as a two-phase mixture of the defect fluorite and the pyrochlore crystal structures. These occur outside of the pyrochlore phase stability fields in the thermal and compositional directions respectively. The defect fluorite and pyrochlore crystal structures are closely related to the fluorite crystal structure since both are oxygen-anion-deficient variations that necessarily account for charge neutrality in the crystal when doping Zr^{4+} sites with RE^{3+} ions (single O^{2-} vacancy per RE^{3+} pair). The most important distinction between the defect fluorite and pyrochlore crystal structures in the context of this work is the ordering of cations (RE^{3+} and Zr^{4+}) and anion vacancies (O^{2-}) in the pyrochlore crystal structure, and the lack thereof in the defect fluorite crystal structure [18]. It is the ability of these rare earth zirconate compounds to exist in equilibrium in several crystal structures at high temperatures that has attracted attention to these materials.

Early research on the rare earth zirconates focused on the structure-property relationship in the area of high-temperature ionic conductivity due to the use of these materials as electrolytes in solid oxide fuel cell applications. Ionic conductivity in the rare earth zirconates is typically determined via frequency-dependent complex impedance spectroscopy, and generally follows an Arrhenius-like temperature dependence at fixed composition. At a given temperature in the compositionally-variant $xNdO_{1.5}$-$(1-x)ZrO_2$ system, a sharp drop in ionic conductivity is observed at the onset of ordering in the pyrochlore crystal structure relative to measured values at compositions corresponding to the defect fluorite structure [19]. While the activation energy for oxygen anion migration in the defect fluorite crystal structure was found to be higher than that of the pyrochlore crystal structure, the pre-exponential factor related to the number of charge carriers was significantly higher for the former relative to the latter, resulting in a decrease in ionic conductivity upon ordering. The structure-property relationship is well characterized for the high-temperature ionic conductivity of the rare earth zirconates. The electronic (i.e. electrons and holes) contribution to the conductivity in direct current measurements however, is less widely discussed. Perhaps a differing level of interest in the use of the rare earth zirconates as high temperature electrode and electrolyte materials is responsible for this distinction. Rare earth zirconates have been considered candidate electrode materials for magnetohydrodynamic power generation, and direct current (DC) conductivity measurements on the $xNdO_{1.5}$-$(1-x)ZrO_2$ system have been reported [20] with ionic transference numbers ranging from 0.17-0.20 for compositions corresponding to the pyrochlore crystal structure in the temperature range 1073-1873 K [21]. In this context, ionic transference number is defined as the ratio of current carried by electrons/holes to the total current carried by all charge carriers (including ions). Despite what may be considered a negligible electronic contribution to the DC conductivity from a viewpoint focused on high-temperature electrode materials selection, mobile electrons could play an important role in the optical properties of the rare earth zirconates. The possibility of free carriers in plasma-sprayed $Nd_2Zr_2O_7$ at high temperatures and their effect on the optical properties of the material are the subject of Chapter 4.

References

1. J. Yen, M. Nicol, “Temperature dependence of the ruby luminescence method for measuring high pressures,” Journal of Applied Physics **72**, 5535-5538 (1992).

2. M. D. Chambers, D. R. Clarke, “Doped oxides for high-temperature luminescence and lifetime thermometry,” Annual Review of Materials Research **39**, 325-329 (2009).
3. K. W. Schlichting, K. Vaidyanathan, Y. H. Sohn, E. H. Jordan, M. Gell, N. P. Padture, “Application of Cr^{3+} photoluminescence piezo-spectroscopy to plasma-sprayed thermal barrier coatings for residual stress measurement,” Materials Science and Engineering A **291**, 68-77 (2000).
4. K. S. Gibson, “The effect of temperature upon the absorption spectrum of a synthetic ruby,” Physical Review **8**, 38-47 (1916).
5. G. F. Imbusch, W. M. Yen, “Ruby – solid state spectroscopy’s serendipitous servant,” in *Lasers, Spectroscopy, and New Ideas*, W. M. Yen, M. D. Levenson, eds. (Springer, 1987), pp. 248-267.
6. E. L. Nichols, H. L. Howes, “The transformation spectrum of the ruby,” in *Proceedings of the National Academy of the Sciences* **15**, 139-145 (1928).
7. T. Kushida, “7B4-Absorption and emission properties of optically pumped ruby,” IEEE Journal of Quantum Electronics **QE-2(9)**, 524-531 (1966).
8. D. M. Brown, A. M. Brown, A. H. Willitsford, R. Dinello-Fass, M. B. Airola, K. M. Siegrist, M. E. Thomas, Y. Chang, “Lidar measurements of solid rocket propellant fire particle plumes,” Applied Optics **55(17)**, 4657-4669 (2016).
9. R. M. Springer, M. E. Thomas, “Transmittance derived line width and line shift in polycrystalline Nd:YAG,” Applied Optics **55(31)**, C1-C8 (2016).
10. L. L. Hench, J. K. West, “The sol-gel process,” Chemical Reviews **90**, 33-72 (1990).

11. C-.J. Li, A. Ohmori, “Relationships between microstructure and properties of thermally sprayed deposits,” Journal of Thermal Spray Technology **11(3)**, 365-374 (2002).
12. R. R. Alfano, *The Supercontinuum Laser Source* (Springer, 2006).
13. M. Kumar, M. N. Islam, F. L. Terry, Jr., M. J. Freeman, A. Chan, M. Neelakandan, T. Manzur, “Stand-off detection of solid targets with diffuse reflection spectroscopy using a high-power mid-infrared supercontinuum source,” Applied Optics **51(15)**, 2794-2807 (2012).
14. P. Kubelka, F. Munk, “Ein beitrag zur optik der farbansriche,” Zeitshrift fur Technische Physik **12**, 593-601 (1931).
15. M. M. Gentleman, D. R. Clarke, “Concepts for luminescence sensing of thermal barrier coatings,” Surface and Coating Technology **188-189**, 93-100 (2004).
16. L. Fukshansky, N. Kazarinova, “Extension of the Kubelka-Munk theory of light propagation in intensely scattering materials to fluorescent media,” Journal of the Optical Society of America **70(9)**, 1101-1111 (1980).
17. M.A. Subramanian, G. Aravamudan, G.V. Subba Rao, “Oxide Pryochlores – A Review,” Progress in Solid State Chemistry **15**, 55-143 (1983).
18. C. Wang, M. Zinkevich, F. Aldinger, “Phase Diagrams and Thermodynamics of Rare-Earth-Doped Zirconia Ceramics,” Pure and Applied Chemistry **79(10)**, 1731-1753 (2007).
19. T. Van Dijk, K.J. De Vries, A.J. Burggraaf, “Electronic Conductivity of Fluorite and Pyrochlore $Ln_xZr_{1-x}O_{2-x/2}$ (Ln = Gd, Nd) Solid Solutions,” Physica Status Solidi (a) **58**, 115-125 (1980).

20. R.A. Chapman, D.B. Meadowcroft, A.J. Walkden, “Some Properties of Zirconates and Stannates with the Pyrochlore Structure,” Journal of Physics D: Applied Physics **3**, 307-319 (1970).
21. M. Guillou, J. Millet, M. Asquiedge, N. Busson, M. Jacquin, S. Palous, M. Pithon, A. Lecante, “Propriétés Électroniques A Haute Température Du Systéme Zircone-Oxyde De Néodyme,” Revue Internationale Des Hautes Températures Et Des Réfractaires **4**, 273-280 (1967).

Chapter 2: Temperature-dependent, diffuse reflectance spectroscopy of plasma-sprayed, Cr-doped, α-alumina using supercontinuum laser illumination and CO_2 laser heating

1. Introduction

In this chapter, ~1 mm thick Cr-doped α-alumina samples were prepared by deposition of sol-gel-derived powders using atmospheric plasma spray (APS), followed by substrate removal and heat-treatment of the resulting monolith. For the as-sprayed and monolithic Cr-doped aluminas, room-temperature phase identification was performed using X-ray diffraction (XRD) while confirmation of doping was done using integrating-sphere diffuse reflectance spectroscopy. Diffuse reflectance measurements were achieved at high temperatures via front-side supercontinuum laser illumination and back-side CO_2 laser heating to probe the temperature dependence of the U-band ($^4A_2 \rightarrow {}^4T_2$) absorption in the Cr-doped α-alumina monoliths. The temperature dependencies of photoemission and absorption corresponding to R′ ($^2T_1 \rightarrow {}^4A_2$, $^4A_2 \rightarrow {}^2T_1$), R ($^2E \rightarrow {}^4A_2$, $^4A_2 \rightarrow {}^2E$) and several vibrationally-shifted R-bands from the Cr-doped α-alumina monoliths were also simultaneously recorded using a spatially-resolved grating spectrometer. This chapter shows the utility of laser-based spectroscopy for investigating the temperature-dependent diffuse reflectance of doped metal oxides and provides insight into the use of these materials for high temperature optical remote sensing applications.

2. Materials and methods

2.1. Synthesis of monolithic Cr-doped (0.1 mol %) α-alumina

2.1.1. Sol-gel preparation of Cr-doped (0.1 mol %) alumina powders suitable for atmospheric plasma spray (APS)

A solid, Al-containing metalorganic compound (Al isopropoxide, ≥ 98 %) was first uniformly suspended in isopropanol using an IKA T25 ULTRA-TURRAX dispersion mixer. With the addition of aqueous dopant solution (Cr(III) nitrate nonahydrate, ≥ 98.5 %) under continued mixing, the Al isopropoxide precursor gradually undergoes a hydrolysis reaction to form a Cr-doped alumina hydrate gel. Following aging for 24 h, the Cr-doped alumina hydrate gel was dried at 373 K for a period of 24 h to remove any organic byproduct and ball-milled using a Roalox alumina-fortified jar/alumina media. In preparation for APS, the Cr-doped alumina hydrate powder was then calcined in an alumina crucible at 1473 K (2 h in air) for thermal conversion to Cr-doped alumina, ball-milled once again, and passed through a 120 mesh (125 μm) sieve. The use of an Al isopropoxide/isopropanol suspension inhibited hydrolysis reaction kinetics to allow for continued physical mixing of the Cr-doped suspension during gradual gelation. This proved critical in producing chemically-uniform Cr-doped alumina powders, which is of utmost importance when measuring optical properties on plasma-sprayed coatings using numerous instruments with various beam sizes.

2.1.2. Atmospheric plasma spray (APS) deposition of Cr-doped (0.1 mol %) alumina powders on C/C composite and subsequent heat-treatment

An APS system consisting of a Metco 9MB plasma gun, Bay State Surface Technologies Model 1200 powder feeder and Yaskawa Motoman HP20 robot movement was used for deposition of the sol-gel-derived Cr-doped alumina powders on CCAT standard laminate C/C composite. APS deposition conditions in Ar/H_2 plasma are reported in Table 1. Rather thick (~1 mm) coatings were produced to ensure the integrity of the Cr-doped α-alumina monoliths after removal of the substrate using thermal oxidation (1073 K, 12 h in air) [1] and subsequent heat-treatment (1973 K, 4 h in air). All heating and cooling ramps used in the synthesis of the monoliths were carried out at a rate of 5 K/min in a horizontal alumina tube furnace with an alumina crucible.

Table 1. Atmospheric plasma spray (APS) deposition conditions for sol-gel-derived Cr-doped (0.1 mol %) alumina powders in Ar/H_2 plasma.

Voltage (V)	Current (A)	Working Distance (mm)	Traverse Speed (mm/s)	Step Size (mm)
70	500	69.85	416.56	3.175

2.2. Room-temperature materials characterization

2.2.1. X-ray diffraction (XRD)

XRD was used for phase identification of the as-sprayed and monolithic Cr-doped aluminas. A Philips X'Pert Pro MRD equipped with a Cu-Kα X-ray source and a programmable divergence slit was used to hold the irradiated length constant at 8 mm throughout the full scan range, thereby increasing the signal-to-noise ratio for high-angle diffraction peaks. Since X-ray irradiated ruby is known to exhibit color change [2], crystallographic structural information was determined via XRD following all spectroscopic measurements.

2.2.2. Scanning electron microscopy (SEM)

An FEI Scios Dual Beam SEM was used to obtain surface micrographs of the Cr-doped aluminas after carbon-coating. Sputtering of carbon on the surface of the samples was performed following all spectroscopic measurements to avoid undesirable absorption from organic contamination.

2.2.3. Integrating-sphere diffuse reflectance spectroscopy

Confirmation of doping in the Cr-doped aluminas was performed on a PerkinElmer Lambda 950 UV-VIS integrating-sphere spectrometer (250-860 nm) at 1 nm optical resolution using NIST-calibrated Spectralon as a reference. Room-temperature, total-integrated diffuse reflectance spectra obtained with this commercial integrating-sphere spectrometer were compared to solid-angle-limited diffuse reflectance spectra measured using the supercontinuum laser illumination source in validating the laser-based technique.

Mid- to long-wave infrared (MWIR-LWIR) total-integrated diffuse reflectance spectra were also collected at room temperature with a PerkinElmer Spectrum 100 FT-IR integrating-sphere spectrometer (4.2-13.7 μm) at 2 cm^{-1} resolution using diffuse gold as a reference and averaged over at least 25 scans. These measurements motivated the choice of the CO_2 laser (10.6 μm) as a heating method and enabled the calculation of temperature-dependent, band-averaged emissivity values for the Cr-doped aluminas (Section 6.2).

2.2.4 Bidirectional reflectance distribution function (BRDF)

In this work, angularly-limited diffuse reflectance measurements about the specular reflection direction were made to gather spectra for the Cr-doped α-alumina monoliths. For calibration purposes, this approach requires that the material being optically characterized must have the same (or nearly the same) scattering characteristics as the reference – Spectralon for this work. This was established with room-temperature, in-plane BRDF measurements using a HeNe laser (633 nm) [3]. Results are shown in Fig. 1 where the near-Lambertian character of scatter from a Cr-doped α-alumina monolith is seen.

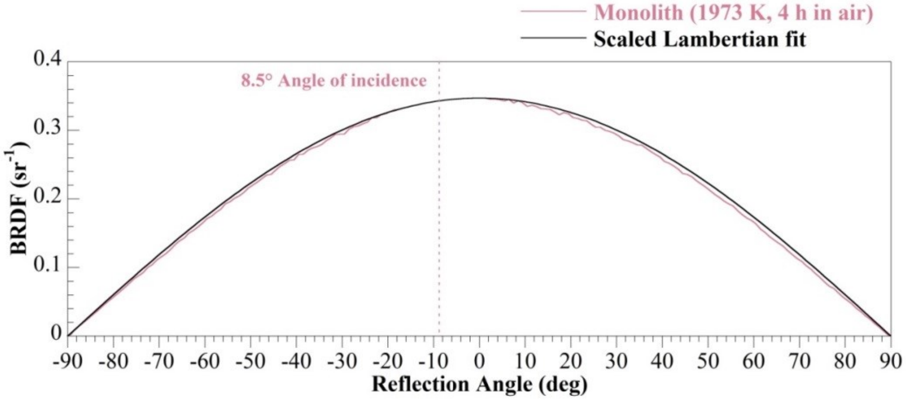

Fig. 1. The angular (relative to the sample surface normal) distribution of back-scattered visible laser light (HeNe, 633 nm) from the Cr-doped α-alumina monolith confirms the near-Lambertian scattering character of these materials. Omitted data points from -17.5-1.5° are due to blocking of the incident HeNe laser beam by the detector during its hemispherical traverse.

2.3. Temperature-dependent diffuse reflectance spectroscopy – visible to near-infrared (VIS-NIR)

2.3.1. Experimental description

An NTK Photonics SuperK EXTREME RED 80 MHz VIS supercontinuum laser (400-2400 nm, 1200 mW nominal visible power) was employed as a directed broadband illumination source for the temperature-dependent diffuse reflectance measurements. The supercontinuum laser was aligned with a 10° angle of incidence to the sample surface normal (Fig. 2) and the scattered light was collected using a plano-convex lens focused onto a 1000 μm step-index multimodal visible/near-infrared optical fiber. Alignment of the collection optics to the specular reflection direction was achieved by back projection of a low-power, fiber-coupled red laser through the collection optics and onto a silver mirror placed at the sample location. This allowed for alignment of the collection optics for concentricity with the visible supercontinuum laser illumination spot and collinearity with the specular reflection direction. A vise-grip alumina mount functioned as a sample holder, and this mount was capable of translation along the sample surface normal to ensure that the front surfaces of samples being measured were correctly aligned with the optical path. Broadband diffuse reflectance spectra were obtained by pairing the collection optics with a fiber-coupled StellarNet EPP2000-UV+VIS grating spectrometer (250-860 nm) having a 25 μm slit and an optical resolution of <1 nm. The detector integration time for the grating spectrometer was 50 ms and spectra were averaged over 100 consecutive measurements.

Laser heating was achieved with a tunable (0-40 W nominal) SYNRAD Firestar CO_2 laser (10.6 μm) and an Agema Thermovision 900 LWIR camera (4.2-13.7 μm) was used for sample surface temperature determination. Laser heating was conducted in air and sample absorbance was high at 10.6 μm (Fig. 9), so an infrared window was not needed for the LWIR camera viewing port on the optical chamber (Fig. 2). The LWIR camera also aided in alignment of the CO_2 and supercontinuum lasers for concentricity by viewing the hot-spots produced by the CO_2 laser and the transmitted diode pump laser for this particular supercontinuum laser source (1064 nm) on a plasma-sprayed Mn-doped α-alumina monolith, synthesized for this purpose. While the hot-spots produced by the CO_2 laser and the transmitted diode pump laser power were essentially the same size (~2 mm diameter), the illuminated spot projected through the collection optics and onto the sample with the low-power, fiber-coupled red laser was significantly larger (~9 mm diameter). Consequently, temperature-dependent diffuse reflectance spectra were collected from the CO_2-laser-heated region as a whole and the reported temperatures for each spectrum represent an average over the heated region. Appropriate filters were used with the collection optics to ensure that the thermal radiation background did not contribute to the measured spectra. The effect of supercontinuum laser beam path optics (e.g., mirrors, filters, lenses, optical fibers), as well as the spectral response of the grating spectrometer detector, on measured spectra were taken into account by measuring the system response using a NIST-calibrated Spectralon standard. The stability of the supercontinuum laser and the accuracy of the temperature-dependent diffuse reflectance spectra are discussed in Section 6.1.

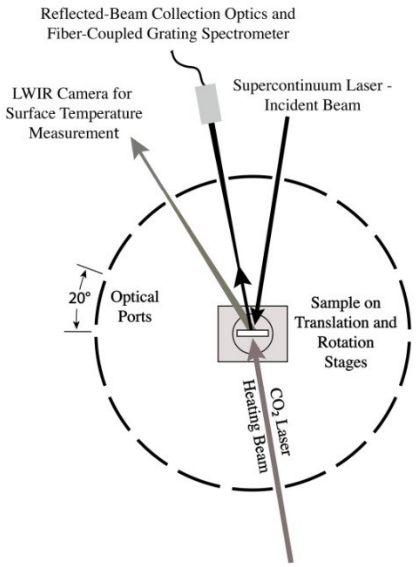

Fig. 2. Schematic of the black-coated optical chamber used for temperature-dependent diffuse reflectance spectroscopy showing the orientations of the various laser sources and instrumentation relative to the sample surface normal. The supercontinuum laser was aligned with a 10° angle of incidence to the sample surface normal and collection optics (paired to a fiber-coupled grating spectrometer) were trained to the specular reflection direction. Concentricity was achieved between the supercontinuum laser and the collection optics as well as between the supercontinuum laser and the CO_2 laser. A LWIR camera aided in CO_2 laser alignment and was used for sample surface temperature determination via pyrometry.

3. Results

3.1. Room-temperature materials characterization

Visual inspection of the as-sprayed and monolithic Cr-doped aluminas (Figs. 3a and 3b) showed that these materials were off-white and pink respectively indicating the impact that heat treatment had on their optical properties. These observations are quantified in the room-temperature, total-integrated (integrating-sphere) diffuse reflectance spectra (Fig. 4) and are intimately related to the phase content of the materials

(Fig. 5). XRD measurements in Fig. 5 indicate that the as-sprayed Cr-doped alumina coating is mixed phase, with both α-alumina and the transitional phase η-alumina being present. It should be noted that it can be difficult to differentiate between the structurally-similar γ- and η-alumina phases based on XRD measurements (especially when peaks are broad due to nanocrystallinity) [4]. Even so, XRD peak locations for the as-sprayed Cr-doped alumina coating more closely match those of η-alumina. Following thermal oxidation of the substrate (1073 K, 12 h in air) and subsequent heat-treatment (1973 K, 4 h in air) the Cr-doped alumina monolith undergoes a phase transformation to consist primarily of the α-alumina phase (Fig. 5). The characteristic Y ($^4A_2 \rightarrow ^4T_1$), B ($^4A_2 \rightarrow ^2T_2$), U ($^4A_2 \rightarrow ^4T_2$), R′ ($^4A_2 \rightarrow ^2T_1$), R ($^4A_2 \rightarrow ^2E$) and two-electron ultraviolet ($^4A_2 \rightarrow ^4T_1$) absorption bands from the Cr^{3+} ion in octahedral coordination [5] are apparent in the room-temperature, total-integrated diffuse reflectance spectrum of the Cr-doped α-alumina monolith (Fig. 4). In contrast, interpretation of the spectrum for the mixed-phase material in the as-sprayed Cr-doped alumina coating is less straightforward (Fig. 4). However, some idea of the coordination polyhedra and the oxidation states of the dopant in the mixed-phase, as-sprayed Cr-doped alumina coating can be inferred from the phase-dependent, total-integrated diffuse reflectance spectra of the various single-phase, Cr-doped transitional aluminas [6]. The U-band in the mixed-phase, as-sprayed Cr-doped alumina coating is observed to lessen in intensity and red-shift with respect to the corresponding absorption in the Cr-doped α-alumina monolith. The Y-band in the mixed-phase, as-sprayed Cr-doped alumina coating is partially-masked by the appearance of a relatively strong absorption centered at 367 nm. Based on the findings of Shen *et al.* [6], these effects can be attributed to the presence of both nanocrystalline Cr-doped η-alumina (Cr^{3+} ion having octahedral, quasi-octahedral and tetrahedral coordination) and Cr^{6+} ions in the form of chromium trioxide [7]. While interesting, the most important aspect of this initial characterization is that the Cr-doped α-alumina monolith is phase stable and should exhibit reversible changes to its optical properties during subsequent characterization at elevated temperatures.

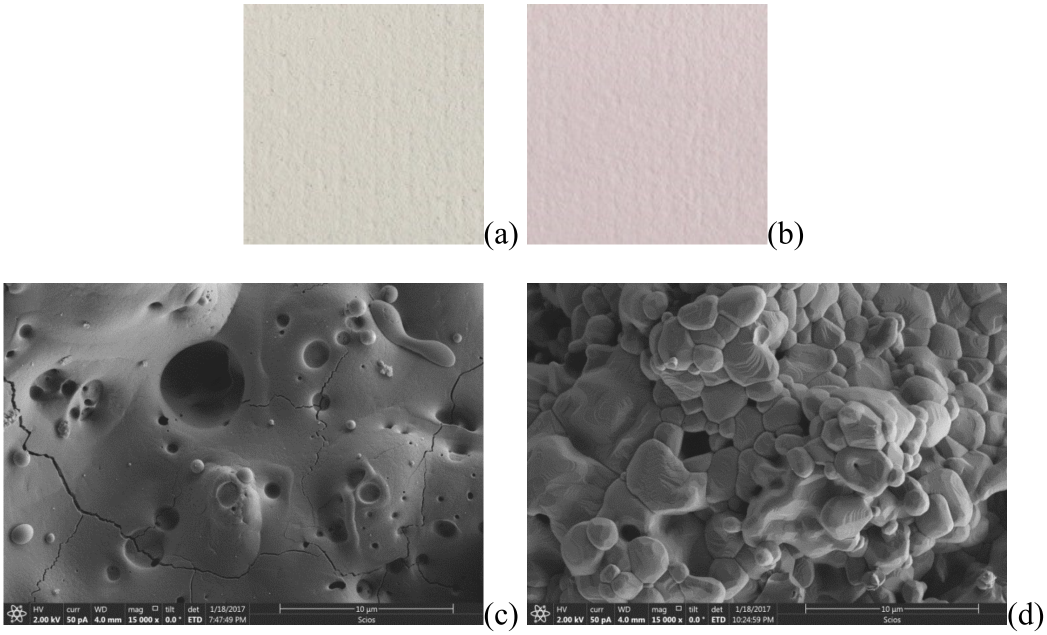

Fig. 3. The visible appearances of the (a) as-sprayed (off-white) and (b) monolithic (pink) Cr-doped aluminas indicate differences in optical absorption that may be correlated to changes in crystallographic structure that occur upon heat-treatment (1973 K, 4 h in air). Scanning electron microscopy (SEM) of the mixed-phase (i.e. α- and η-alumina), as-sprayed Cr-doped alumina coating (c) and the Cr-doped α-alumina monolith (d) shows that grain growth, an emergence of crystal faceting and a generation of intragranular optical scatterers (pores) are all associated with the transformation of η-phase to the α-alumina host.

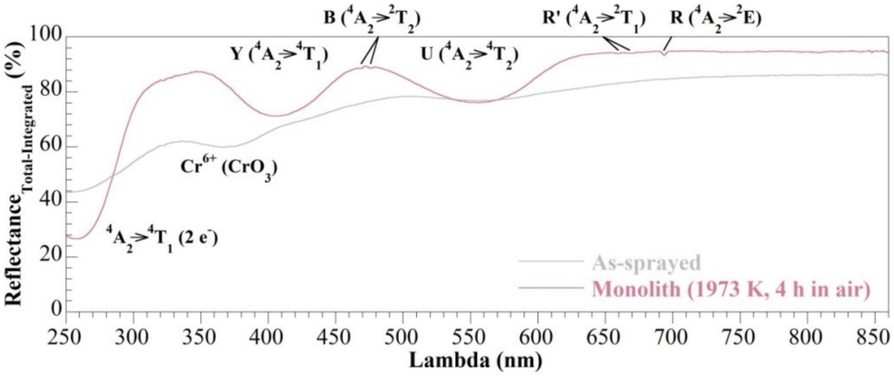

Fig. 4. The well-defined Y, B, U, R′, R and two-electron ultraviolet absorption bands in the room-temperature, total-integrated (integrating-sphere) diffuse reflectance spectrum (8° angle of incidence) of the Cr-doped α-alumina monolith correspond to the Cr^{3+} ion in octahedral coordination, whereas the relatively featureless absorptive character of the as-sprayed coating is suggestive of a mixed phase (i.e. α and η) alumina deposit with several coordination polyhedra (i.e. octahedron, quasi-octahedron and tetrahedron) and dopant oxidation states (i.e. Cr^{3+} and Cr^{6+}).

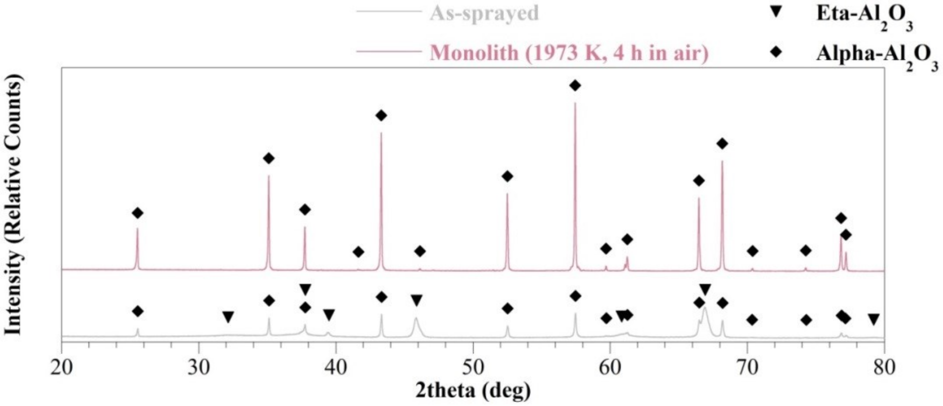

Fig. 5. X-ray diffraction patterns of the as-sprayed and monolithic Cr-doped aluminas showing locations of diffraction peaks associated with various crystallographic structures of alumina. The top scan corresponds to the Cr-doped α-alumina monolith and the bottom scan relates to the mixed-phase, as-sprayed Cr-doped alumina coating (i.e. α- and η-alumina).

3.2. Temperature-dependent diffuse reflectance spectroscopy – visible to near-infrared (VIS-NIR)

Supercontinuum-laser-based spectroscopy, paired with a spatially-resolved grating spectrometer, provides unique insight into the simultaneous temperature dependence of the intimately related absorption (pump) and photoemission (fluorescence) bands. A room-temperature comparison is shown in Fig. 6a of the total-integrated (integrating-sphere) diffuse reflectance spectrum and the angularly-limited (supercontinuum-laser-based) diffuse reflectance spectrum for the Cr-doped α-alumina monolith. Agreement between the commercial (integrating-sphere) and experimental (supercontinuum-laser-based) diffuse reflectance spectra in the area of the green U-band ($^4A_2 \rightarrow {}^4T_2$) absorption is quite good, and confirms the validity of the approach taken in this work. In the red region of the supercontinuum-laser-based measurement, photoemission from R′ ($^2T_1 \rightarrow {}^4A_2$), R ($^2E \rightarrow {}^4A_2$) and the vibrationally-shifted R-band [8] is also simultaneously observed owing to the use of a spatially-resolved grating spectrometer. For this reason, we have chosen to present the full spectral breadth (510-840 nm) of each temperature-dependent diffuse reflectance spectrum, as opposed to showing the temperature dependence of each absorption/emission feature separately.

Temperature dependence is readily observable in Fig. 6b for the photoemission from R′, R and the vibrationally-shifted R-band. Photoemission from the R-band experiences thermal quenching and a slight red-shift with increasing temperature (Fig. 6b). A single configuration coordinate model for the thermal quenching based on thermalization of the $^4T_2$ (U) energy level to a crossover point of higher energy state within the ground level ($^4A_2$) and subsequent nonradiative relaxation to the energetic minima of $^4A_2$ via phonon coupling has been suggested [9]. Stated simply, above 640 K, relaxation from the U-level to the ground state is dominated by nonradiative relaxation methods as opposed to the radiative electronic transition that results in R-band fluorescence at lower temperatures ($^2E \rightarrow ^4A_2$). Laser heating of the Cr-doped α-alumina monolith from room-temperature to 770 K also causes the U-band absorption to shift slightly towards the red and broaden asymmetrically (Fig. 6b). This same effect has been reported previously for the optical transmission spectra of synthetic ruby up to 703 K [10]. In addition, it is interesting to note that the R′, R and the vibrationally-shifted R-band can be observed in absorption above 770 K (Figs. 6b and 6c) even though photoemission was observed at lower temperatures (Figs. 6a and 6b). This is likely a result of depopulation of the $^4T_2$ (U) level via the thermal quenching mechanism which at lower temperatures efficiently relaxes to populate the $^2T_1$ (R′) and ^2E (R) levels [11], from which the R′, R and vibrationally-shifted R-band photoemissions originate, respectively. It is assumed that the additional spectral width on the short wavelength-side of the vibrationally-shifted R-band observed in absorption for spectra above 770 K includes the R-band absorption.

Above 890 K the U-band absorption appears to be split (Fig. 6c). The U-band absorption is actually comprised of the ||-component (incident light propagating parallel to the c-axis [12]) and the ⊥-component (incident light propagating perpendicular to the c-axis [12]). The combined effect of both the ||- and the ⊥-component are observed due to the random orientation of α-alumina crystallites in the monolith, and it appears that these components follow different temperature dependencies. This splitting of the U-band absorption becomes pronounced at temperatures above 890 K, and the ||-component of the U-band absorption continues to slightly red-shift and asymmetrically vibrationally-broaden with increasing temperature. A blending of the U-band ||-component and the R′-

band absorptions is apparent above 890 K. Also appearing above 890 K is a broad absorption band which exists largely within the 760-810 nm region, but is unidentifiable based on single-frequency shifts in the energy level structure of the Cr^{3+} ion in octahedral coordination. Based on the Raman spectra of ruby, it has been suggested that bands appearing in this region may be attributed to electronic transitions within the octahedrally-coordinated Cr^{3+} ion which have been Stokes-shifted by combinations of vibrational frequencies in the α-alumina host [8].

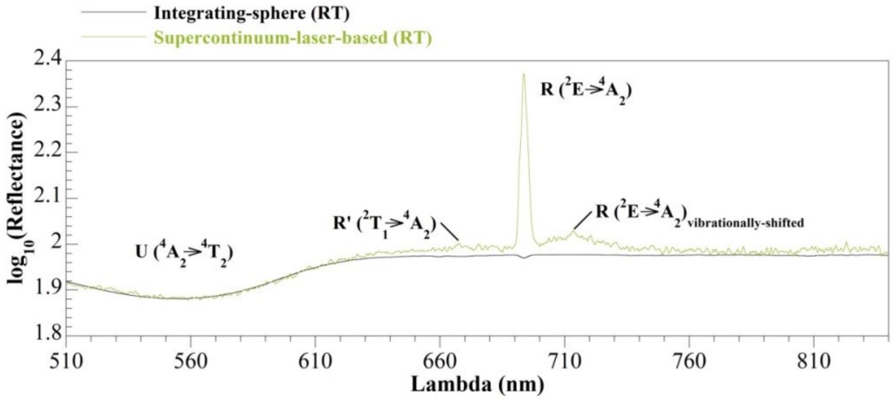

(a)

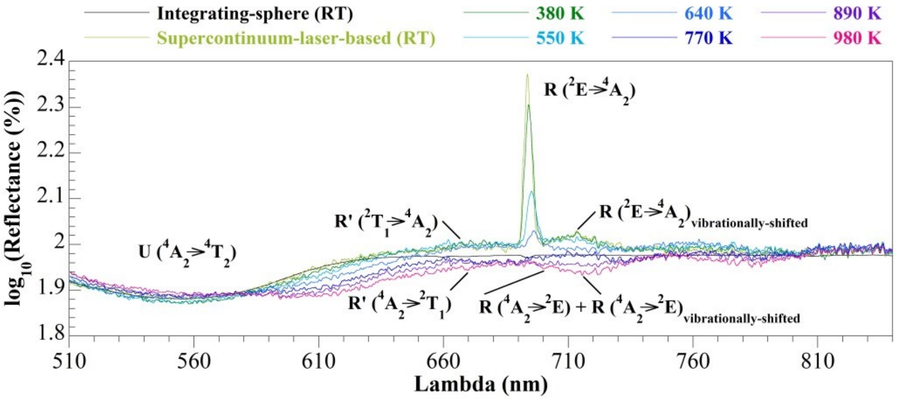

(b)

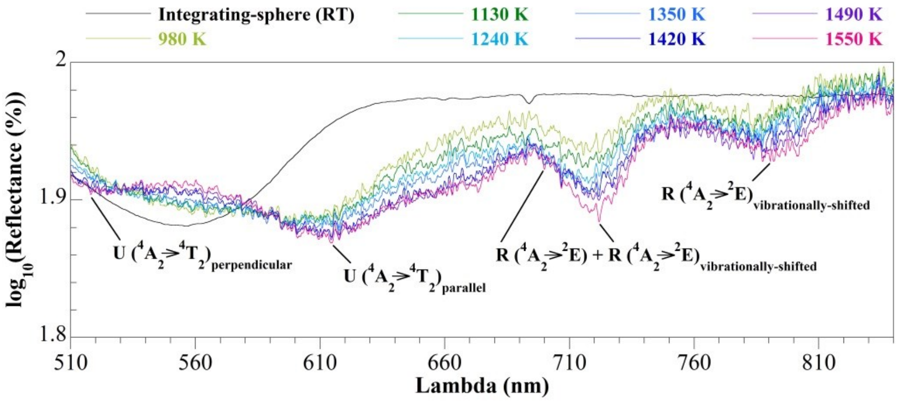

(c)

Fig. 6. Diffuse reflectance (10° angle of incidence) spectroscopy of the Cr-doped α-alumina monolith up to ((a) and (b)) and significantly above (c) ~900 K shows a multitude of thermally-activated phenomena, most notable being the previously unobserved splitting of the U-band ($^4A_2 \rightarrow {}^4T_2$) absorption for octahedrally-coordinated Cr^{3+} above 890 K. This observation may be due to thermal and optical anisotropy in the α-alumina crystallites.

4. Discussion

It is well known that the α-alumina phase is thermodynamically stable to the melt (2345 K). Seldom discussed, however, is the temperature dependence of the coefficient of thermal expansion (CTE) for the a- and c-axes in α-alumina. Temperature-dependent XRD measurements made by Kondo *et al.* on ruby up to 1173 K [13] have been extrapolated to similar measurements made by Ishizawa *et al.* on sapphire at 2170 K [14] and have shown a preferential thermal expansion along the c-axis of the undoped (sapphire) and doped (ruby) α-alumina single crystals. This effect was attributed by Kondo *et al.* to the temperature dependence of the cation intermetallic repulsion forces for face-sharing octahedra, where the shortest distance between cations lies along the c-axis [13]. We analyzed the data tabulated by Kondo *et al.* for the temperature dependence of the ruby CTE and identified a significant deviation from linearity starting at 900 K for the c-axis. This analysis involved performing a linear fit on the tabulated dataset using an incrementally-increasing number of the reported data points and calculating the L2-norm of the linear fit residuals. When data points above 900 K were included in the linear fit the deviation from linearity significantly increased for the c-axis (i.e. above 900 K is a fairly non-linear regime for the temperature dependence of the CTE for the c-axis).

As such, splitting of the U-band absorption above 890 K (Figs. 6b and 6c) is likely a combined effect of thermal and optical anisotropy in the α-alumina crystallites. Anisotropy of this nature could result in splitting of the U-band absorption, as octahedrally-coordinated Cr^{3+} ions in α-alumina crystallites with their c-axes oriented in the direction of supercontinuum laser illumination would be subjected to a rapidly changing crystal field as viewed by the incident photon. In comparison, the incident photon would view the change in the crystal field around the octahedrally-coordinated Cr^{3+} ions as more gradual if the α-alumina crystallites were positioned with their a-axes oriented in the direction of supercontinuum laser illumination. Similarly, if the crystal fields along each of these directions are weakening at different rates, then the temperature-dependent wavelength shifts for the ǁ- and ⊥-components of the U-band absorption will occur at correspondingly different rates, resulting in band splitting. Interestingly, in 1928 Nichols and Howes' observed that "when a ruby is heated it turns black as viewed by reflected light, and the transmitted light loses the ruddy color characteristic of this material when cold" [15]. In their work, this comment was linked to a specific “transformation” temperature of 873 K. The effects noted in this work at temperatures above 890 K appear to agree with Nichols and Howes’ earlier work.

The combination of front-side supercontinuum laser illumination with back-side CO_2 laser heating appears to be a powerful tool for temperature-dependent diffuse reflectance spectroscopy of doped metal oxides. While thermal instability of the supercontinuum laser photonic crystal fiber tip can lead to a spatial wavering of the laser beam and subsequent radiometric fluctuation of collected light, this issue can be mitigated by careful alignment of the collection optics, thermal insulation of the coiled photonic crystal fiber and averaging over successive spectra. It should be noted that the spectral breath of the supercontinuum laser used in this work (400-2400 nm) extends into the short-wave infrared (SWIR), and since NIR-SWIR grating spectrometers are readily available, this technique could be extended from VIS-NIR to NIR-SWIR frequencies which are important for characterization of the temperature-dependent absorption/emission bands in rare-earth-doped metal oxides with closely-spaced energy levels for electronic transition [16]. In theory, with proper CO_2 laser power selection, laser-based diffuse reflectance spectroscopy could be used to study the optical properties of doped metal oxides to the melt, but issues with material radiative relief will likely be encountered as the thermal boundary for high-temperature solid-state spectroscopy is approached. It should be emphasized that the choice of physical form for the doped metal oxide used in this work (plasma-sprayed monolith) was far from inconsequential; more traditional physical forms of Cr-doped α-alumina such as dense pressed pellets readily thermally-shocked and fractured under CO_2 laser heating below 890 K.

With respect to the use of Cr-doped α-alumina for high-temperature remote sensing applications, the optical absorptions/emissions from the green to longer visible wavelengths, which are well-spaced and distinct at room temperature, are significantly blended up to 1550 K by a multitude of physical processes (Fig. 6c). Most pronounced of these thermally-activated blending phenomena is the splitting of the U-band absorption in the octahedrally-coordinated Cr^{3+} ion above 890 K (Fig. 6b). This change in the absorption characteristics essentially blends the green and red optical absorptions with increasing temperature and leaves little to no spectral window for identification of distinguishable absorption/emission features in the visible for Cr-doped α-alumina above 1550 K. The absorption feature centered at 721.44 nm resulting from blending of the R-band and the vibrationally-shifted R-band in Cr-doped α-alumina is most prominent at 1550 K (Fig. 6c).

5. Conclusion

A thoughtful approach for the synthesis of Cr-doped α-alumina monoliths in a physical form suitable for laser heating has been developed by pairing of sol-gel and thermal spray technologies. These porous monoliths have allowed for investigation of a laser-based technique for temperature-dependent diffuse reflectance spectroscopy involving front-side supercontinuum laser illumination and back-side CO_2 laser heating. Temperature-dependent diffuse reflectance spectra have revealed a multitude of previously unobserved thermally-activated phenomena in Cr-doped α-alumina, most notable being the splitting of the U-band ($^4A_2 \rightarrow {}^4T_2$) absorption for octahedrally-coordinated Cr^{3+} above 890 K. A mechanism for the splitting of the U-band absorption based on thermal and optical anisotropy in the α-alumina crystallites has been proposed. Physics-based modeling of this effect in Cr-doped α-alumina will be the subject of future work with the ultimate goal of developing models to predict the optical behavior of other dopants in the same α-alumina host at high temperature.

6. Supplemental material

6.1. Supercontinuum laser stability and accuracy of reported spectra

The stability of the supercontinuum laser source was assessed by means of time-resolved measurement of diffusely-reflected laser light from NIST-calibrated Spectralon at room temperature. Following initial emission, measurements were obtained in 0.5 h increments for a period of 3.5 h, and the raw spectra are shown in Fig. 7. While the supercontinuum laser provides significant power to 400 nm on the short wavelength-side of its specified output (400-2400 nm), the optics used in this work resulted in a loss of usable power below ~490 nm. Based on the measurements provided in Fig. 7, the supercontinuum laser thermally equilibrates to a practical extent after a period of 1 h from initial emission, and a quantitative treatment of the source stability from 1-3.5 h is presented in Fig. 8 by ratio of each subsequent measurement to the spectrum obtained at 1 h. The useful measurement range (490-860 nm) is further limited to a stability window of 510-840 nm by radiometric fluctuation of the supercontinuum laser in the 490-510 nm wavelength region and the spectral response of the grating spectrometer detector from 840-860 nm. A statistical analysis over the stability window for each of the measurements in Fig. 8 is displayed in Table 2. After a source warm-up period of 1 h, diffusely-reflected supercontinuum laser light from a NIST-calibrated Spectralon served as a reference spectrum for temperature-dependent diffuse reflectance measurements on the Cr-doped α-alumina monoliths over the following 2.5 h. The results given here support the accuracy of the spectra reported in Fig. 6.

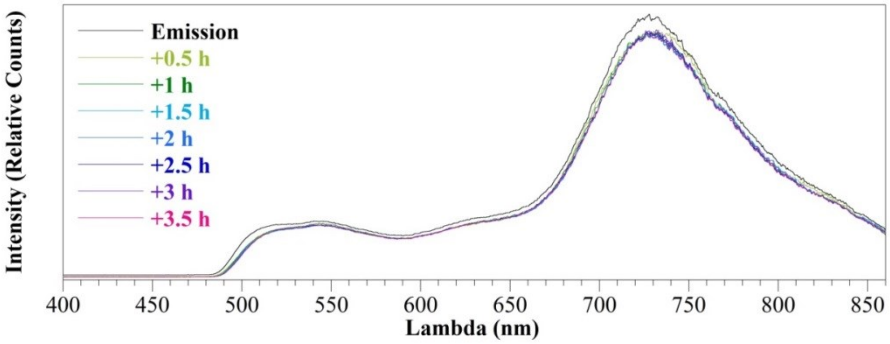

Fig. 7. Time-resolved measurement of diffusely-reflected supercontinuum laser light from NIST-calibrated Spectralon. This figure qualitatively shows that the source thermally equilibrates to a practical extent after a period of 1 h from initial emission. A useful measurement range of 490-860 nm is established by a loss of usable power below ~490 nm due to the optics used in this work.

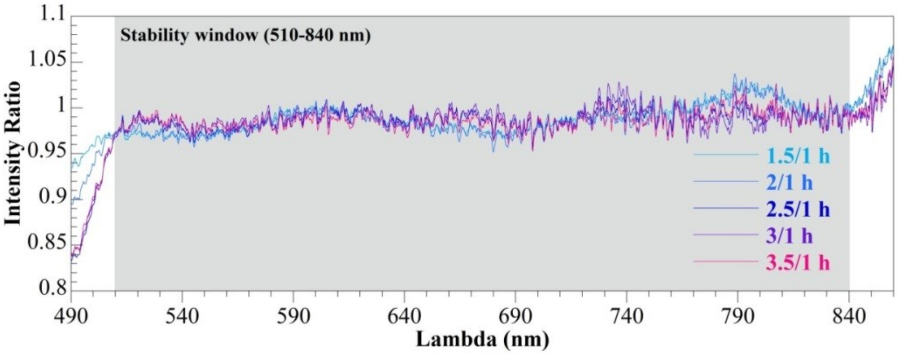

Fig. 8. The useful measurement range of 490-860 nm used in this work is further limited to a stability window of 510-840 nm by the radiometric fluctuation of the supercontinuum laser in the 490-510 nm region as well as by the spectral response of the grating spectrometer detector from 840-860 nm.

Table 2. Statistical analysis of the supercontinuum laser intensity ratio.

	1.5/1 h	2/1 h	2.5/1 h	3/1 h	3.5/1 h
Average	0.9896	0.9873	0.9882	0.9892	0.9869
STD	0.0147	0.0155	0.0100	0.0105	0.0099

6.2. Band-averaged emissivity calculation for sample surface temperature correction

Accurate values for emissivity are needed over the wavelength range used for infrared measurements (4.2-13.7 μm) in order to estimate the various temperatures the sample surface attains during laser heating. For the results presented here, temperature-dependent, band-averaged emissivity values for the as-sprayed and monolithic Cr-doped aluminas were calculated using Eqs. 1-3:

$$\varepsilon_{band-averaged,material}(T) = \frac{\int \varepsilon_{material}(\nu) SRF_{LWIR\ camera}(\nu) L_{BB}(\nu,T) d\nu}{\int SRF_{LWIR\ camera}(\nu) L_{BB}(\nu,T)\, d\nu} \quad (1)$$

$$\varepsilon_{material}(\nu) = 1 - R_{material}(\nu, \theta_i = 0) \quad (2)$$

$$L_{BB}(\nu,T) = \frac{2h\nu^3 c^2}{\exp\left(\frac{hc\nu}{k_B T}\right) - 1} \quad (3)$$

In Eqs. 1-3, $R_{material}(\nu, \theta_i = 0)$, $SRF_{LWIR\ camera}(\nu)$ and $L_{BB}(\nu,T)$ are frequency-dependent parameters (cm^{-1}) and correspond to the room-temperature, total-integrated diffuse reflectance of the material with normal illumination (Fig. 9), the LWIR camera spectral response function (SRF, Fig. 9) and the black-body spectral radiance, respectively. Temperature-dependent, band-averaged emissivity calculations of this nature rely on two assumptions, the first being that the transmittances of the thick (~1 mm) Cr-doped aluminas are negligible over the LWIR camera bandwidth, and the second being an insignificant temperature dependence of the optical constants of the materials in this region. It should be noted that the frequency-dependent, near-normal emittance of sapphire (single crystal α-alumina) is largely independent of temperature in this wavelength range when viewed along the c-axis [17] and this supports the second assumption. The results of the temperature-dependent, band-averaged emissivity calculations are presented in Fig. 10 in 100 K increments from 293-1593 K, along with the mean band-averaged emissivity of the Cr-doped aluminas. The mean band-averaged emissivity of the Cr-doped α-alumina monolith was used for correction of sample surface temperatures determined via LWIR camera pyrometry. Emissivity-corrected sample surface temperatures were averaged over the hot-spot produced by CO_2 laser heating via a full-width tenth-maximum (FWTM) condition that defined the heated zone quite well. This average temperature is reported for each temperature-dependent diffuse reflectance spectrum reported in Fig. 6.

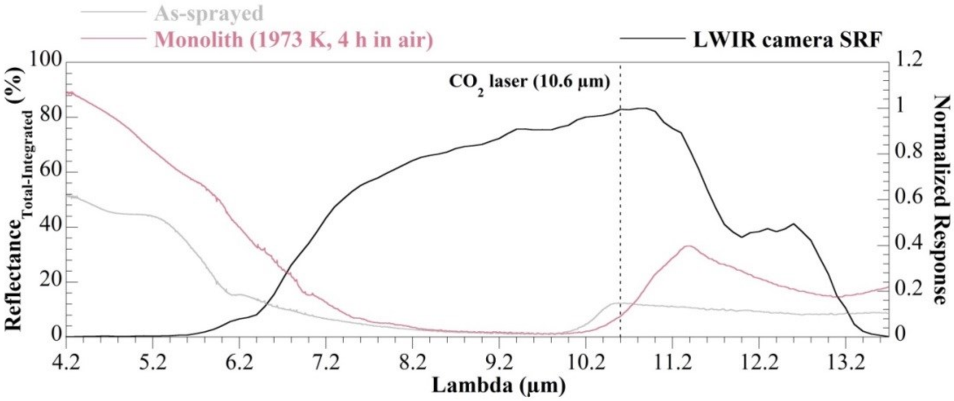

Fig. 9. Comparison of the room-temperature, total-integrated (integrating-sphere) diffuse reflectance spectra (normal illumination) for the as-sprayed and monolithic Cr-doped aluminas with the Spectral Response Function (SRF) of the LWIR camera shows the materials are near-black-body over a large portion of the LWIR camera band.

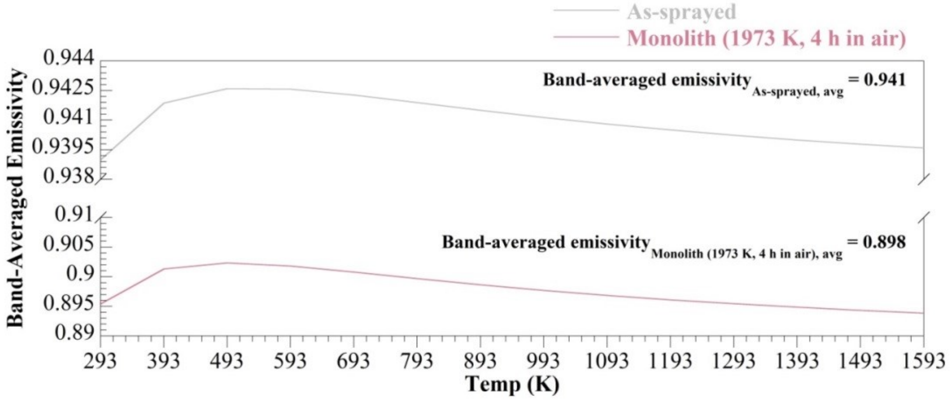

Fig. 10. Temperature-dependent, band-averaged emissivities for the as-sprayed and monolithic Cr-doped aluminas are calculated in the range of 293-1593 K. As variation of band-averaged emissivity with temperature is seen to be small, mean band-averaged emissivity over this temperature range was used for correction of sample surface temperatures obtained via LWIR camera pyrometry.

References

1. L. Wang, J. I. Eldridge, S. M. Guo, "Thermal radiation properties of plasma-sprayed $Gd_2Zr_2O_7$ thermal barrier coatings," Scripta Materialia **69**, 674-677 (2013).
2. D. R. Mason, J. S. Thorp, "Evidence for existence of Cr^{2+} and Cr^{4+} in x-irradiated ruby," in *Proceedings of the Physical Society* **87**, 49-53 (1966).
3. A. M. Brown, D. V. Hahn, M. E. Thomas, D. M. Brown, J. Makowski, "Optical material characterization through BSDF measurement and analysis," in *Proceedings of SPIE* **7792**, 779211 (2010).
4. D. S. Maciver, H. H. Tobin, R. T. Barth, "Catalytic aluminas I. surface chemistry of eta and gamma alumina," Journal of Catalysis **2**, 485-497 (1963).
5. T. Kushida, "7B4-Absorption and emission properties of optically pumped ruby," IEEE Journal of Quantum Electronics **QE-2(9)**, 524-531 (1966).
6. L. Shen, C. Hu, S. Zhou, A. Mukherjee, Q. Huang, "Phase-dependent photoluminescence of Cr-doped alumina phosphors," Optical Materials **35**, 1268-1272 (2013).
7. C. P. Poole, Jr., J. F. Itzel, Jr., "Optical reflection spectra of chromia-alumina," The Journal of Chemical Physics **39(12)**, 3445-3455 (1963).
8. R. S. Krishnan, "Raman spectrum of alumina and the luminescence of ruby," in *Proceedings of the Indian Academy of Sciences – Section A* **26**, 450-459 (1947).
9. Z. Zhang, K. T. V. Grattan, A. W. Palmer, "Temperature dependences of fluorescence lifetimes in Cr^{3+}-doped insulating crystals," Physical Review B **48(11)**, 7772-7778 (1993).

10. K. S. Gibson, "The effect of temperature upon the absorption spectrum of a synthetic ruby," Physical Review **8**, 38-47 (1916).

11. J. T. Verdeyen, *Laser Electronics*, 3rd ed., (Prentice Hall, 1995).

12. T. H. Maiman, R. H. Hoskins, I. J. D'Haenens, C. K. Asawa, V. Evtuhov, "Stimulated optical emission in fluorescent solids. II. Spectroscopy and stimulated emission in ruby," Physical Review **123(4)**, 1151-1157 (1961).

13. S. Kondo, K. Tateishi, N. Ishizawa, "Structural evolution of corundum at high temperatures," Japanese Journal of Applied Physics **47(1)**, 616-619 (2008).

14. N. Ishizawa, T. Miyata, I. Minato, F. Marumo, S. Iwai, "A structural investigation of α-Al_2O_3 at 2170 K," Acta Crystallographica B **36**, 228-230 (1980).

15. E. L. Nichols, H. L. Howes, "The transformation spectrum of the ruby," in *Proceedings of the National Academy of the Sciences* **15**, 139-145 (1928).

16. M. D. Chambers, D. R. Clarke, "Doped oxides for high-temperature luminescence and lifetime thermometry," Annual Review of Materials Research **39**, 325-329 (2009).

17. M. E. Thomas, P. S. Wayland, D. H. Terry, "Imaging pyrometry of oxides," in *Proceedings of SPIE* **3361**, 2-13 (1998).

Chapter 3: Interpretation of supercontinuum laser diffuse reflectance spectroscopy measurements using extended Kubelka-Munk theory

1. Introduction

In Chapter 2 a technique was developed for temperature-dependent diffuse reflectance spectroscopy of monolithic plasma-sprayed deposits via supercontinuum laser illumination and CO_2 laser heating [1]. Owing to the broadband spectral nature of the supercontinuum source [2] and analysis of diffusely-reflected laser light with a spatially-resolved grating spectrometer, we have simultaneously observed U-band ($^4A_2 \rightarrow {}^4T_2$) absorption and R'- ($^2T_1 \rightarrow {}^4A_2$) , R- ($^2E \rightarrow {}^4A_2$) and vibrationally-shifted R-band fluorescence in monolithic Cr-doped α-alumina [1,3]. Measurements of diffuse reflectance $R(\lambda)$ that include information about the temperature dependence of the fluorescence bands can be fit with the Kubelka-Munk (K-M) theory extended to include fluorescence. The extended K-M model includes source terms and, consequently, is an inhomogeneous analog to the standard K-M theory. Among others, Bonham has developed a solution to the inhomogeneous differential equation for the case of polychromatic diffuse light illumination and an infinitely thick sample approximation [4]. The principal result of Bonham's work is an expression for $R(\lambda)$ as a function of only the normalized illumination source $I_{0,norm}(\lambda)$, the K-M absorption $K(\lambda)$ and back-scattering $S(\lambda)$ coefficients, and the quantum efficiency $Q_e(\lambda)$. In this chapter, we have fit temperature-dependent $R(\lambda)$ spectra for monolithic Cr-doped α-alumina using the extended K-M model with $Q_e(\lambda)$ as the fitting parameter. These temperature-dependent $R(\lambda)$ spectra were measured using supercontinuum laser diffuse reflectance spectroscopy, and thus contain fluorescent components. This chapter will serve to investigate the utility of pairing supercontinuum laser diffuse reflectance measurements with the extended K-M model for determination of temperature-dependent quantum efficiencies in materials that can be obtained in diffusely-reflecting physical forms.

2. Materials and Methods

The specific details of the procedures used in the synthesis of the Cr-doped α-alumina monoliths can be found in earlier work [1]. Some of the processing details previously presented are of particular relevance to the scope of this work. These are briefly described below. Alumina powder doped with 0.1 mol % Cr was synthesized using sol-gel technologies, and subsequently plasma-sprayed on C/C composite to a coating thickness of ~1 mm. Following removal of the substrate using thermal oxidation (1073 K, 12 h in air), the Cr-doped monoliths were heat-treated for conversion to α-alumina (1973 K, 4 h in air). All spectroscopic measurements presented in this work were made on these Cr-doped α-alumina monoliths. The angularly-resolved scattering characteristics of the Cr-doped α-alumina monoliths were investigated by means of in-plane bidirectional reflectance distribution function measurement [5]. These measurements used a 633 nm HeNe laser as an illumination source and confirmed the near-Lambertian scattering characteristics of the Cr-doped α-alumina monoliths [1].

In applying the extended K-M model, we make use of two measurement techniques for diffuse reflectance spectroscopy. The first measurement technique is the commercial integrating-sphere spectrometer determination of $R(\lambda)$ at room temperature. Due to the double-monochromator arrangement of these integrating-sphere spectrometers, R'-, R- and vibrationally-shifted R-band fluorescence are not captured despite the usual occurrence of U-band absorption (i.e. $R(\lambda) < 1$ at all wavelengths). In fact, the electronic transitions responsible for R'- ($^2T_1 \rightarrow {}^4A_2$) and R-band fluorescence ($^2E \rightarrow {}^4A_2$) are measured in absorption with these instruments. The supercontinuum laser diffuse reflectance measurements described in the previous chapter differ significantly from the integrating-sphere $R(\lambda)$ spectra [1]. In the context of this work, the most important distinction between these measurement techniques is that $R(\lambda)$ as determined with the supercontinuum laser can exceed unity. That is, supercontinuum source illumination and analysis of diffusely-reflect laser light with a spatially-resolved grating spectrometer must include fluorescent contributions if $R(\lambda) > 1$. This is evident in the Fig. 11, which shows a room-temperature comparison of $R(\lambda)$ for these two measurement techniques for the Cr-doped α-alumina monolith [1].

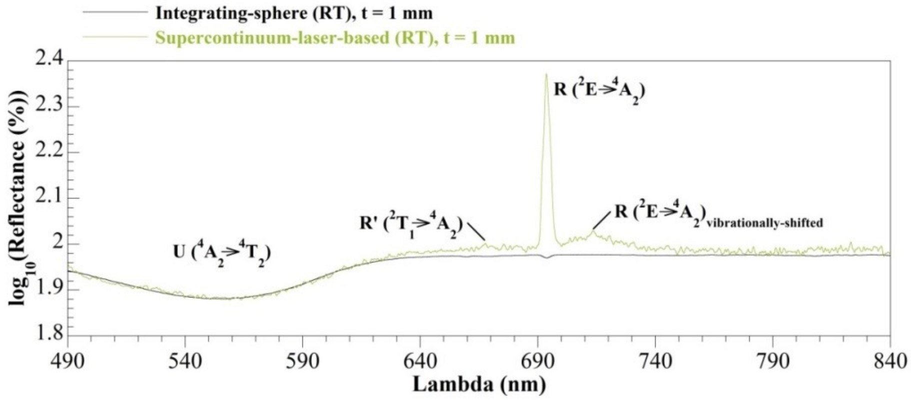

Fig. 11. A room-temperature comparison of the integrating-sphere diffuse reflectance and that measured with the supercontinuum laser for the Cr-doped α-alumina monolith highlights an important distinction between these two measurement techniques – the diffuse reflectance $R(\lambda)$ can exceed unity for the supercontinuum-lased-based measurements owing to induced fluorescence (reproduced from Ref. 1).

The temperature-dependent diffuse reflectance spectra for the Cr-doped α-alumina monolith in Fig. 12 form the basis of our investigation into the utility of the extended K-M model for determining $Q_e(\lambda)$ [1]. From Fig. 12, it is apparent that the strength of the U-band absorption is relatively stable over the temperature range of our measurements (room temperature to 640 K). However the R-band fluorescence, comprised of the $^{2}\mathrm{E}\rightarrow{}^{4}\mathrm{A}_2$ electronic transition and its vibrationally-shifted counterpart, undergoes significant thermal quenching up to 640 K. A physical mechanism for the thermal quenching of the R-band fluorescence has been proposed [6]. Our interest lies however not in the physical mechanism governing the thermal quenching of R-band fluorescence, but in establishing a methodology for determining the temperature dependence of the quantum efficiency in polycrystalline materials such as Cr-doped α-alumina. In this particular instance, we aim to characterize the quantum efficiency of the fluorescence for the R'-, R- and vibrationally-shifted R-band as a single entity.

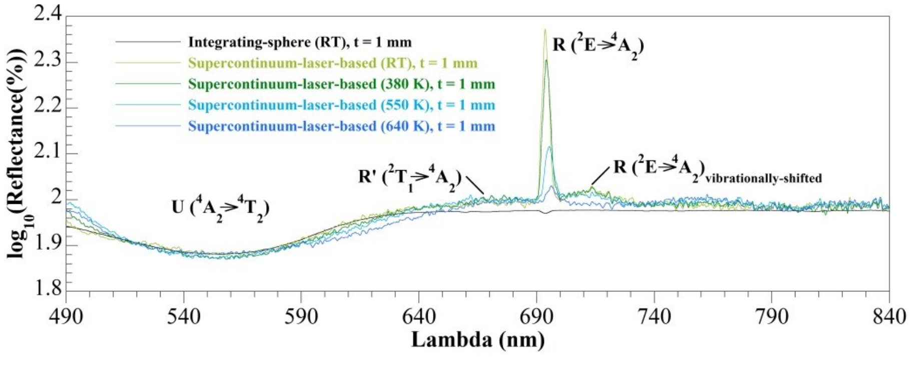

Fig. 12. A comparison of the room-temperature integrating-sphere diffuse reflectance to results obtained using the supercontinuum laser at elevated temperatures for the Cr-doped α-alumina monolith. The strength of the U-band absorption is relatively stable from room-temperature to 640 K. The R-band fluorescence however undergoes significant thermal quenching (reproduced from Ref. 1).

3. Results

3.1. The extended Kubelka-Munk (K-M) model for monolithic Cr-doped α-alumina and supercontinuum laser illumination

We now consider the extended K-M model developed by Bonham for $R(\lambda)$ in highly-scattering and fluorescent media, applicable for an infinitely-thick-sample approximation ($t = \infty$) with polychromatic illumination [4]:

$$R(\lambda) = \left(1 + \frac{K(\lambda)}{S(\lambda)} - \frac{A(\lambda)}{S(\lambda)}\right) + \left(2 + \frac{K(\lambda)}{S(\lambda)} - \frac{A(\lambda)}{S(\lambda)}\right)\left(\frac{Q_e(\lambda)}{2I_{0,norm}(\lambda)}\right)\int_{\lambda_1'}^{\lambda_2'}\left(\frac{K_d(\lambda')I_0(\lambda')}{A(\lambda) + A(\lambda')}\right)\left(2 + \frac{K(\lambda')}{S(\lambda')} - \frac{A(\lambda')}{S(\lambda')}\right)d\lambda' \quad (1)$$

where

$$A(\lambda) = \sqrt{(K(\lambda) + S(\lambda))^2 - S(\lambda)^2} \quad (2)$$

$$A(\lambda') = \sqrt{(K(\lambda') + S(\lambda'))^2 - S(\lambda')^2} \quad (3)$$

and

$$K_d(\lambda') = K(\lambda') - K_0(\lambda') \quad (4)$$

In Eq. 1 the wavelengths λ' correspond to the pump absorption band (i.e. 490-650 nm) and the wavelengths λ relate to the spectral regions of fluorescence. The K-M absorption coefficient of the dopant in the spectral region of the pump absorption band, $K_d(\lambda')$, is simply $K(\lambda')$ minus the K-M absorption coefficient for the undoped material, $K_0(\lambda')$. For an ultralow-loss host material such as α-alumina, we assume $K_0(\lambda') = 0$, therefore $K_d(\lambda') = K(\lambda')$. Eq. 1 can be rewritten as:

$$R(\lambda) = \left(1 + \frac{K(\lambda)}{S(\lambda)} - \frac{A(\lambda)}{S(\lambda)}\right) + \left(2 + \frac{K(\lambda)}{S(\lambda)} - \frac{A(\lambda)}{S(\lambda)}\right)\left(\frac{Q_e(\lambda)}{2I_{0,norm}(\lambda)}\right)\int_{\lambda_1'}^{\lambda_2'}\left(\frac{K(\lambda')I_0(\lambda')}{A(\lambda) + A(\lambda')}\right)\left(2 + \frac{K(\lambda')}{S(\lambda')} - \frac{A(\lambda')}{S(\lambda')}\right)d\lambda' \quad (5)$$

It is now clear that $R(\lambda)$ for a highly-scattering and fluorescent medium can be calculated with knowledge of $I_{0,norm}(\lambda)$, $K(\lambda)$, $S(\lambda)$ and $Q_e(\lambda)$ in both the $\lambda'$and λ spectral regions.

To determine $I_{0,norm}(\lambda)$, supercontinuum laser light was diffusely reflected from NIST-calibrated Spectralon at room temperature and gathered with the same collection optics used in the temperature-dependent measurements on the Cr-doped α-alumina monolith [1]. Fig. 13 shows the normalized intensity of the supercontinuum laser source over a broad wavelength range (250-840 nm). The particular supercontinuum laser used in these measurements has specified output power from 400-2400 nm, however the optics employed limited the usable power to above ~490 nm [1]. Therefore, the lower spectral limit of integration for the pump absorption band is chosen as $\lambda_1' = 490\ nm$. The upper spectral limit of integration is chosen as $\lambda_2' = 650\ nm$ based on the pump absorption band spectral content in the integrating-sphere diffuse reflectance measurements on the Cr-doped α-alumina monolith (Fig. 11).

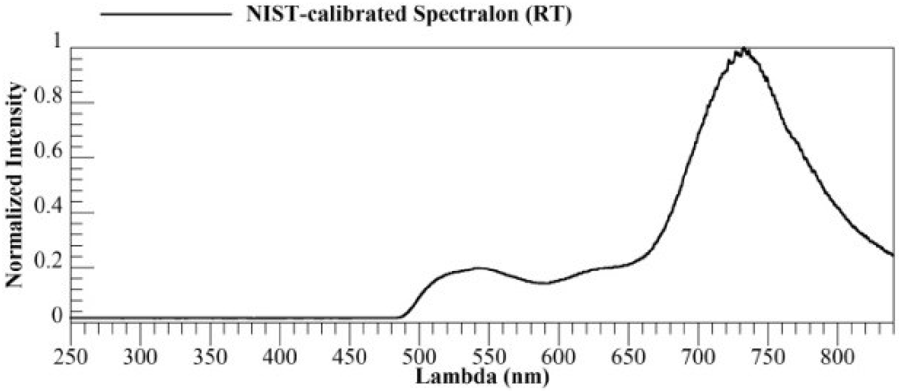

Fig. 13. Diffusely-reflected supercontinuum laser light from room-temperature NIST-calibrated Spectralon is used to characterize the normalized illumination source $I_{0,norm}(\lambda)$, and defines the lower spectral limit of integration for the pump absorption band as $\lambda_1' = 490\ nm$.

3.2. Fitting the extended Kubelka-Munk (K-M) model to temperature-dependent supercontinuum laser diffuse reflectance spectra for monolithic Cr-doped α-alumina

Up to 640 K, a lack of significant temperature dependence in terms of the strength and spectral shift of the pump absorption band and the corresponding fluorescence (Fig. 12) allows us to make a simplifying assumption. Namely, we determine $K(\lambda)$ and $S(\lambda)$ in the λ' and λ spectral regions with a single set of room-temperature integrating-sphere measurements of diffuse reflectance $R(\lambda)$ and transmittance $T(\lambda)$. Accurate values of $K(\lambda)$ and $S(\lambda)$ in both the $\lambda'$and λ spectral regions are important in describing scattering and absorption of incident pump light, as well as scattering and reabsorption of the corresponding fluorescent light. The procedure for determining $K(\lambda)$ and $S(\lambda)$ from $R(\lambda)$ and $T(\lambda)$ is outlined in many papers on the standard K-M theory, but we direct the reader to the work of Fukshansky *et al.* in particular. In Figs. 14 and 15 we present $R(\lambda)$, $T(\lambda)$, $K(\lambda)$, and $S(\lambda)$ for the Cr-doped α-alumina monolith.

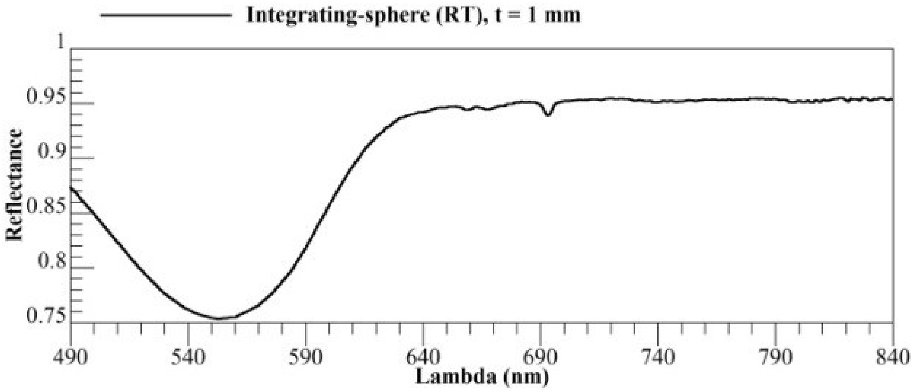

(a)

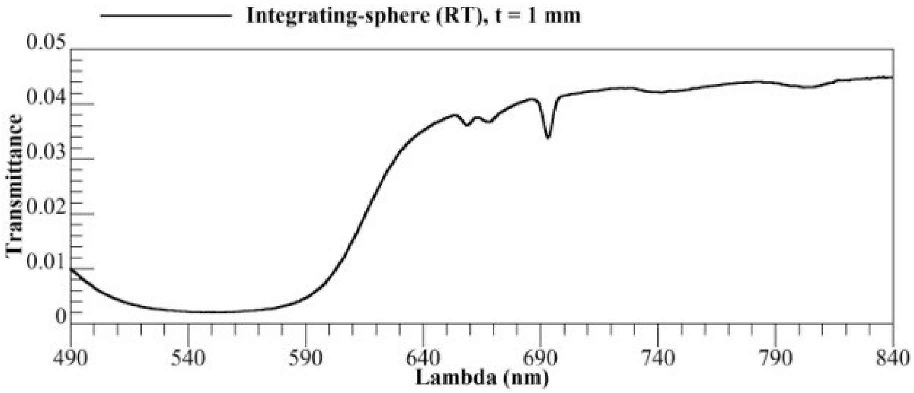

(b)

Fig. 14. Room-temperature integrating-sphere spectrometer measurements of the diffuse reflectance $R(\lambda)$ (a) and transmittance $T(\lambda)$ (b) provide the necessary information for determination of the standard theory K-M absorption $K(\lambda)$ and scattering $S(\lambda)$ coefficients.

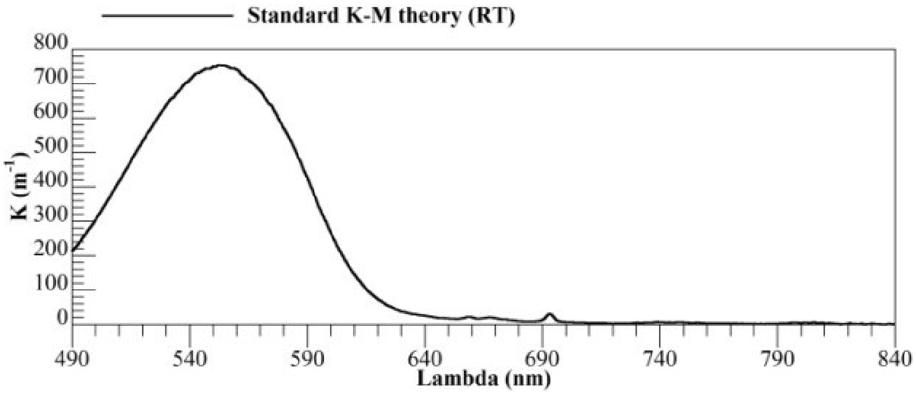

(a)

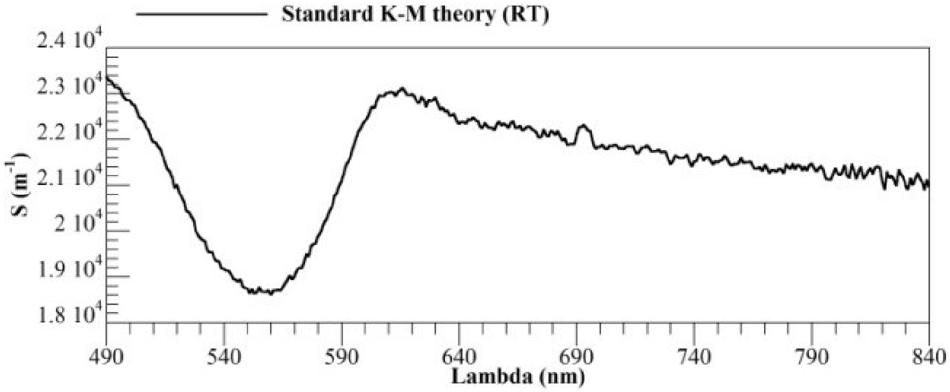

(b)

Fig. 15. The standard theory K-M absorption $K(\lambda)$ (a) and scattering $S(\lambda)$ (b) coefficients are calculated from room-temperature diffuse reflectance $R(\lambda)$ and transmittance $T(\lambda)$ spectra for thickness $t = 1\,mm$.

It is useful to mention that these $K(\lambda)$ and $S(\lambda)$ values can be used to determine the room-temperature diffuse reflectance $R(\lambda)_{t=\infty}|_{Q_e(\lambda)=0}$ for an infinitely-thick Cr-doped α-alumina monolith using Eq. 5 with $Q_e(\lambda) = 0$. The results of such a calculation are shown in Fig. 16.

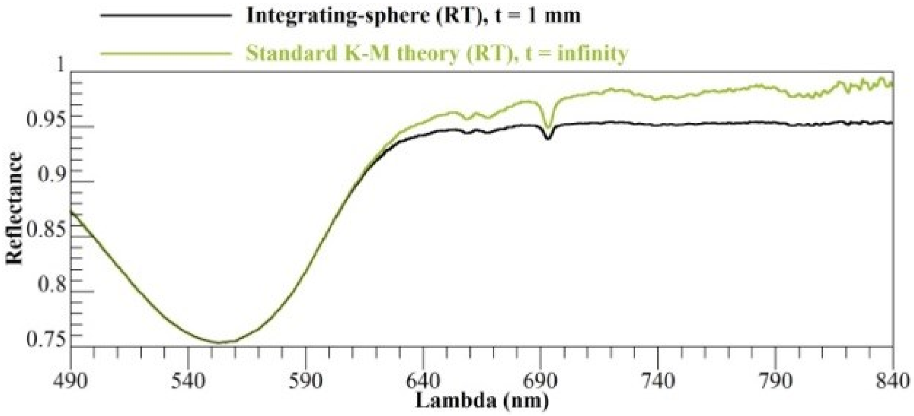

Fig. 16. Comparison of the room-temperature integrating-sphere spectrum of the diffuse reflectance $R(\lambda)$ for thickness $t = 1\,mm$ with $R(\lambda)_{t=\infty}|_{Q_e(\lambda)=0}$ calculated by the standard K-M theory $(Q_e(\lambda) = 0)$ for an infinite thickness.

In fitting the supercontinuum laser diffuse reflectance spectra for the Cr-doped α-alumina monolith (Fig. 12) by use of Eq. 5, we employed an if-while-loop condition with $Q_e(\lambda)$ as the fitting parameter. A logical starting point for calculating $R(\lambda)$ is $R(\lambda)_{t=\infty}|_{Q_e(\lambda)=0}$. This provides assurance that the initial calculated value of $R(\lambda) < 1$. If the measured value of $R(\lambda) > R(\lambda)_{t=\infty}|_{Q_e(\lambda)=0}$, $Q_e(\lambda)$ was increased by a tenth of percent and $R(\lambda)$ was recalculated. This procedure was repeated while the measured value of $R(\lambda)$ was greater than that of $R(\lambda)$ as calculated by Eq. 5. In Fig. 17, the results of fitting the extended K-M model to the temperature-dependent supercontinuum laser diffuse reflectance spectra for the Cr-doped α-alumina monolith are shown. As is shown in Fig. 17, the fluorescence can be fit reasonably well with the extended K-M model.

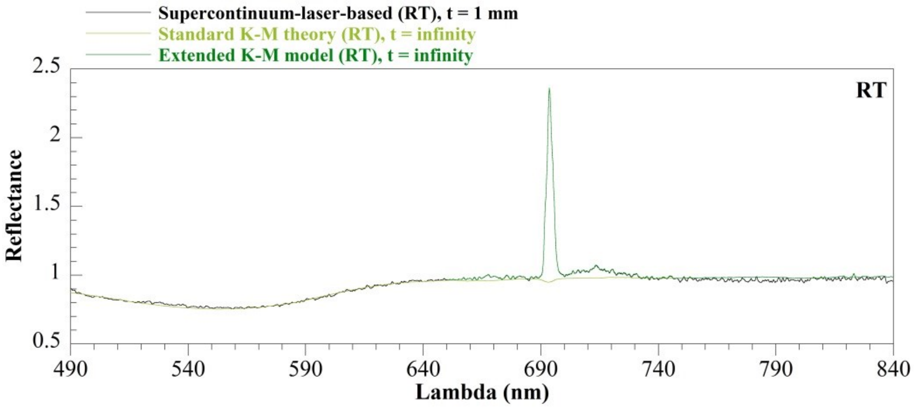
Supercontinuum-laser-based (RT), t = 1 mm
Standard K-M theory (RT), t = infinity
Extended K-M model (RT), t = infinity
RT
Reflectance
2.5
2
1.5
1
0.5
490
540
590
640
690
740
790
840
Lambda (nm)

(a)

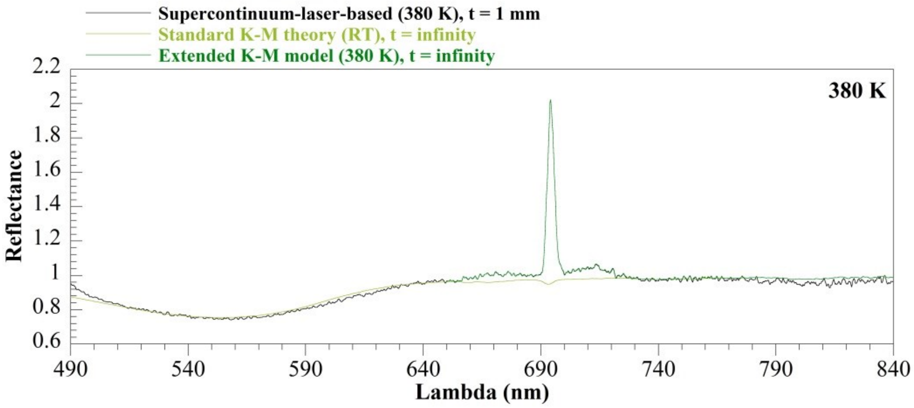
Supercontinuum-laser-based (380 K), t = 1 mm
Standard K-M theory (RT), t = infinity
Extended K-M model (380 K), t = infinity
380 K
Reflectance
2.2
2
1.8
1.6
1.4
1.2
1
0.8
0.6
490
540
590
640
690
740
790
840
Lambda (nm)

(b)

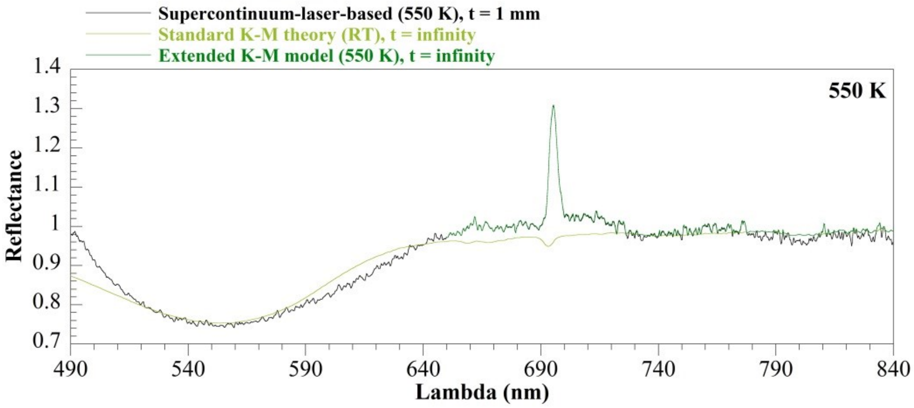
Supercontinuum-laser-based (550 K), t = 1 mm
Standard K-M theory (RT), t = infinity
Extended K-M model (550 K), t = infinity
550 K
Reflectance
1.4
1.3
1.2
1.1
1
0.9
0.8
0.7
490
540
590
640
690
740
790
840
Lambda (nm)

(c)

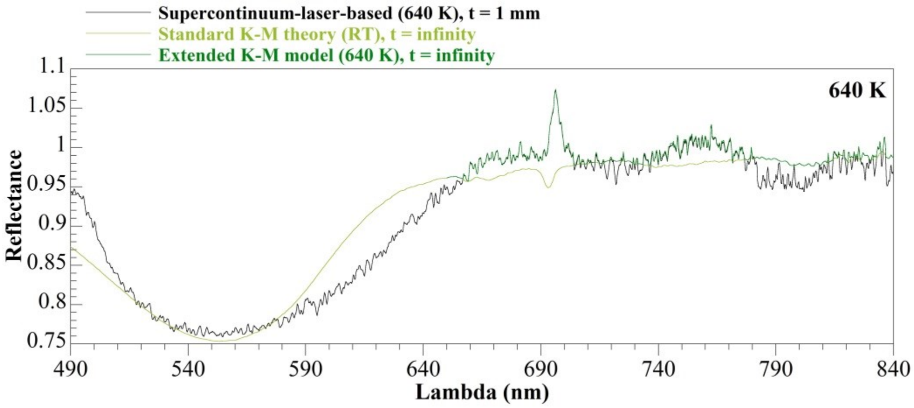

(d)

Fig. 17. The extended K-M model is fit to the temperature-dependent supercontinuum laser diffuse reflectance spectra using the quantum efficiency $Q_e(\lambda)$ as the fitting parameter. In spectral regions devoid of fluorescence, the extended K-M model reduces to the standard K-M theory ($Q_e(\lambda) = 0$).

In the context of the extended K-M model, $Q_e(\lambda)$ is the normalized fluorescence spectral line shape multiplied by the single-valued quantum efficiency $Q_{e_{sv}}$. Hence, the single-valued quantum efficiencies are the maxima of the curve fits $Q_e(\lambda)$. In Fig. 18 we present the single-valued quantum efficiencies as a function of temperature for the Cr-doped α-alumina monolith.

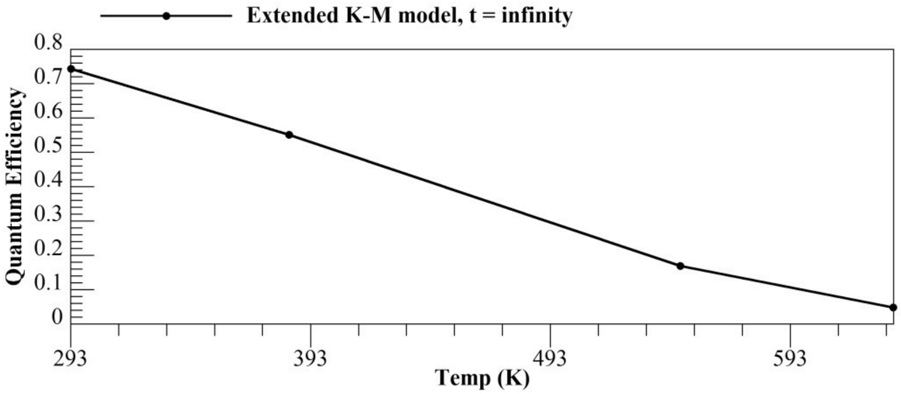

Fig. 18. The temperature-dependence of the single-valued quantum efficiency $Q_{e_{sv}}$ is determined using supercontinuum laser diffuse reflectance spectroscopy and the extended K-M model.

The room-temperature value of $Q_{e_{sv}} = 0.743$ agrees well with $Q_{e_{sv}} \sim 0.7$ for R-band fluorescence in ruby (i.e. single crystal Cr-doped α-alumina) [8]. This statement takes into consideration that we have determined $Q_{e_{sv}}$ for the R'-, R- and vibrationally shifted R-band fluorescence as a single entity. This result also provides confidence in the extended K-M model for determining quantum efficiency.

3.3. Consideration of the high-temperature applicability conditions for the extended K-M model

It would be useful to understand the influence of the temperature dependence of the pump absorption band on the accuracy of the single-valued quantum efficiencies determined by the extended K-M model. Recalling that $R(\lambda)_{t=\infty}|_{Q_e(\lambda)=0}$ was determined using room-temperature values of $K(\lambda)$ and $S(\lambda)$ (Figs. 14 and 15), any inaccuracies in the single-valued quantum efficiencies are likely rooted in the simplifying assumption made regarding the strength of the pump absorption band. Namely, we assumed the strength of the pump absorption band can be described by $R(\lambda)_{t=\infty}|_{Q_e(\lambda)=0}$ at all temperatures, however our supercontinuum laser diffuse reflectance measurements show a measureable change in the spectral characteristics of the pump absorption band with increasing temperature (Fig. 17). A ratio of the strength of the pump absorption band as described by $R(\lambda)_{t=\infty}|_{Q_e(\lambda)=0}$ to that given by $R(\lambda)$ measured with the supercontinuum laser can be used as a metric for determining temperature-dependent changes in the accuracy of the single-valued quantum efficiencies. In Fig. 19 we present this ratio determined by numerical integration of the following:

$$\frac{\int_{\lambda_1'}^{\lambda_2'} 1 - R(\lambda')_{t=\infty}|_{Q_e(\lambda')=0}\, d\lambda'}{\int_{\lambda_1'}^{\lambda_2'} 1 - R(\lambda') d\lambda'} \quad (6)$$

Here we have assumed the transmittance in the spectral region of pump band is negligible for $t = 1\,mm$ (Fig. 14b).

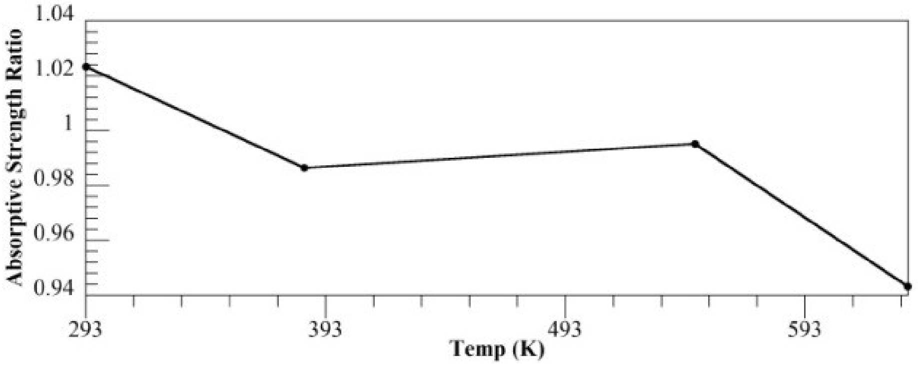

Fig. 19. The temperature dependence of the absorptive-strength ratio has implications for the applicability conditions of the extended K-M model. The absorptive-strength ratio is defined by Eq. 6.

The accuracy of the strength of the pump absorption band as described by $R(\lambda)_{t=\infty}|_{Q_e(\lambda)=0}$ is seen to be on the order of a few percent at all measured temperatures. As temperature increases and the pump absorption band shifts to longer wavelengths outside of the limits of integration, we can expect the accuracy of the single-valued quantum efficiencies determined by the extended K-M model to decrease. For accurate determination of quantum efficiency, it appears the extended K-M model should be applied to cases with negligible temperature dependence for the spectral shift and the strengthening/weakening in the pump absorption band. There should also be neglibigle temperature dependence for the spectral shift in the fluorescence bands to accurately describe reabsorption of the fluorescence. The qualitative applicability condition we have imposed on the extended K-M model for determining high-temperature quantum efficiency could be removed with temperature-dependent knowledge of $R(\lambda)$ and $T(\lambda)$, and therefore $K(\lambda)$ and $S(\lambda)$, as measured with the integrating-sphere spectrometer.

4. Discussion

Beyond fluorescence thermometry, it would be useful to use quantum efficiency as a metric for detection of an unknown fluorescent dopant without any preconceived notion of the spectral regions that constitute the pump absorption and fluorescence bands. If we consider the concept of overall quantum efficiency for all fluorescent and absorbed light, as opposed to the quantum efficiency of a specific fluorescent electronic transition, the following equation can be used to determine the overall quantum efficiency over the full spectral range of measurement:

$$Q_{e_{sv}} = \frac{\int I_n(\lambda) - I_0(\lambda)|_{I_n(\lambda)-I_0(\lambda)>0}}{\int I_0(\lambda) - I_n(\lambda)|_{I_0(\lambda)-I_n(\lambda)>0}} \quad (7)$$

This empirical formulation of the overall quantum efficiency could be particularly useful since it does not require definition of the pump absorption or fluorescence bands. The extended K-M model, described by Eq. 5, does require this definition. In addition, application of Eq. 7 is likely computationally faster and this may have implications for real-time detection of unknown fluorescent dopants. In Eq. 7, $I_n(\lambda)$ represent the intensity spectra for supercontinuum laser light diffusely reflected from a fluorescent medium at time $n > 0$. Supercontinuum laser light diffusely reflected from the non-fluorescent medium at time $n = 0$ is denoted by $I_0(\lambda)$. An empirical formulation of the overall quantum efficiency of this nature relies on the fluorescent dopant being introduced into the non-fluorescent medium at time $n > 0$, and assumes that the introduction of the dopant does not significantly alter the scattering properties of the media in spectral regions far removed from the pump absorption and fluorescence bands. Eq. 7 may have implications for the characterization of aluminized solid rocket propellant fires [1,9].

5. Conclusion

A combination of supercontinuum laser diffuse reflectance spectroscopy together with the extended K-M model has been developed as a methodology for a temperature-dependent determination of quantum efficiency. Analysis of the accuracy of quantum efficiency values resulting from the extended K-M model has provided a qualitative understanding of the high-temperature conditions that can be treated using the extended

K-M model. Beyond model validation, supercontinuum laser diffuse reflectance spectroscopy may be useful for real-time detection of unknown fluorescent dopants.

References

1. M. C. Brupbacher, D. Zhang, W. M. Buchta, M. B. Airola, D. M. Brown, M. E. Thomas, J. B. Spicer, "Temperature-dependent diffuse reflectance spectroscopy of plasma-sprayed Cr-doped α-alumina using supercontinuum laser illumination and CO_2 laser heating," Applied Optics, Under Review (2017).
2. R. R. Alfano, *The Supercontinuum Laser Source* (Springer, 2006).
3. T. Kushida, "7B4-Absorption and emission properties of optically pumped ruby," IEEE Journal of Quantum Electronics **QE-2(9)**, 524-531 (1966).
4. J. S. Bonham, "Fluorescence and Kubelka-Munk theory," Color Research and Application **11(3)**, 223-230 (1986).
5. A. M. Brown, D. V. Hahn, M. E. Thomas, D. M. Brown, J. Makowski, "Optical material characterization through BSDF measurement and analysis," in *Proceedings of SPIE* **7792**, 779211 (2010).
6. Z. Zhang, K. T. V. Grattan, A. W. Palmer, "Temperature dependences of fluorescence lifetimes in Cr^{3+}-doped insulating crystals," Physical Review B **48(11)**, 7772-7778 (1993).
7. L. Fukshansky, N. Kazarinova, "Extension of the Kubelka-Munk theory of light propagation in intensely scattering materials to fluorescent media," Journal of the Optical Society of America **70(9)**, 1101-1111 (1980).
8. J. T. Verdeyen, *Laser Electronic*, 3rd ed., (Prentice Hall, 1995).

9. D. M. Brown, A. M. Brown, A. H. Willitsford, R. Dinello-Fass, M. B. Airola, K. M. Siegrist, M. E. Thomas, Y. Chang, “Lidar measurements of solid rocket propellant fire particle plumes,” Applied Optics **55(17)**, 4657-4669 (2016).

Chapter 4: Determination of high-temperature, infrared spectral reflectance of plasma-sprayed $Nd_2Zr_2O_7$

1. Introduction

Interest in the rare earth zirconates as next-generation thermal barrier coatings has strengthened our understanding of many relevant coating properties such as thermal conductivity [1]. However, a significant void remains in the literature in the area of solid-state spectroscopy with regard to the rare earth zirconates, both in bulk and coating form, as well as at ambient and elevated temperatures. In this chapter, an approach for quantifying the spectral reflectance of next-generation thermal barrier coatings has been investigated and applied to plasma-sprayed $Nd_2Zr_2O_7$. Thick (~1 mm) neodymium zirconate (NZ) monoliths were derived from atmospheric plasma spray (APS) and subsequent heat-treatment. Temperature-dependent diffuse reflectance measurements were obtained in the near- to short-wave infrared (NIR-SWIR) using broadband, supercontinuum-laser illumination and CO_2 laser heating. A physics-based model based on free-carrier effects has been developed to interpret the results of these measurements. Materials characterization of NZ in various physical forms has shown significant structure-optical property relationships which may have implications for selection of spray parameters that will yield coatings with suitable properties for the demands of various applications. Materials characterization included ambient and non-ambient X-ray diffraction (XRD), as well as room-temperature integrating-sphere diffuse reflectance spectroscopy.

2. Materials and methods

2.1. Synthesis of neodymium zirconate (NZ) monoliths

2.1.1. Solid-state preparation of $Nd_2Zr_2O_7$ powders suitable for atmospheric plasma spray (APS)

The $Nd_2Zr_2O_7$ powders used in this work were procured from a commercial supplier (Trans-Tech, Adamstown, MD 21710, USA) and were prepared using traditional solid-state powder processing techniques. The specific processing details are proprietary, although it is likely that the $Nd_2Zr_2O_7$ powders are derived from oxide materials and follow a sequence of blending, calcination, wet-milling, spray-drying and sintering operations [2]. An SEM micrograph of the as-received $Nd_2Zr_2O_7$ powder is shown in Fig. 20. A hollow-spherical morphology typical of spray-dried powders is retained in the sintered particles, and these micron-sized spherical particles are comprised of finer particulates.

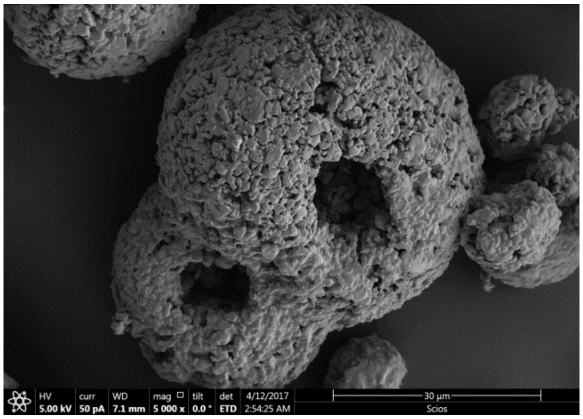

Fig. 20. An SEM micrograph of the as-received $Nd_2Zr_2O_7$ powder showing particles with hollow-spherical morphology and sizing appropriate for atmospheric plasma spray.

2.1.2. Atmospheric plasma spray (APS) deposition of $Nd_2Zr_2O_7$ powders on C/C composite and subsequent heat-treatment

An APS system comprised of a 9MB plasma gun (Oerlikon Metco, Westbury, NY 11590, USA), Model 1200 powder feeder (Bay State Surface Technologies, Auburn, MA 01501, USA) and HP20 robot movement (Yaskawa Motoman, Miamisburg, OH 45342, USA) was used for deposition of the $Nd_2Zr_2O_7$ powders on standard laminate C/C composite (Carbon-Carbon Advanced Technologies, Kennedale, TX 76060, USA). The specific parameters used for APS deposition of these powders in Ar/H_2 plasma are reported in Table 3. Aside from a desire for near-optical-opacity, rather thick (~1 mm) coatings were produced to ensure the integrity of the NZ monoliths after removal of the substrate using thermal oxidation (1073 K, 12 h in air) [3]. All heating and cooling ramps used to synthesize the NZ monoliths were carried out at a rate of 100 K/h in a $MoSi_2/ZrO_2$ air furnace on a zirconia FBD fiber board (Zircar Zirconia, Florida, NY 10921, USA).

Table 3. Atmospheric plasma spray (APS) deposition conditions for Trans-Tech $Nd_2Zr_2O_7$ powders in Ar/H_2 plasma.

Voltage (V)	Current (A)	Working Distance (mm)	Traverse Speed (mm/s)	Step Size (mm)
75	510	63.5	416.56	3.175

2.2. Materials characterization

2.2.1. Scanning electron microscopy (SEM)

A Scios Dual Beam SEM (FEI, Hillsboro, Oregon 97124, USA) was used to obtain micrographs of the as-received $Nd_2Zr_2O_7$ powder after sputtering of a thin iridium coating (see Fig. 20).

2.2.2. X-ray diffraction (XRD)

XRD was used for phase identification of NZ in the as-received $Nd_2Zr_2O_7$ powder, the as-sprayed coating and the monolithic state. For ambient XRD measurements, an X'Pert Pro MRD (Philips, Andover, MA 01810, USA) equipped with a programmable divergence slit was used to hold the irradiated length constant at 8 mm throughout the full scan range to increase the signal-to-noise ratio for high-angle diffraction peaks. Non-ambient XRD measurements were conducted under a cover gas of flowing dry air (100 SCCM) using an Empryean diffractometer (PANalytical, Westborough, MA 01581, USA). This instrument had a fixed divergence slit and was outfitted with an HTK 1200N high-temperature chamber (Anton Paar, Ashland, VA 23005, USA). All heating and cooling ramps were 20 K/min between dwell temperatures. Dwell temperatures correspond to diffraction pattern collection (293-1453 K in 100 K increments). Both diffractometers used Cu-Kα radiation.

2.2.3. Integrating-sphere diffuse reflectance spectroscopy

Room-temperature diffuse reflectance measurements were performed on NZ in various physical forms, including a pressed and sintered pellet derived from the as-received $Nd_2Zr_2O_7$ powder (1973 K, 4 h in air). From the ultraviolet (UV) to the short-wave infrared (SWIR) a Lambda 950 integrating-sphere spectrometer (PerkinElmer, Waltham, MA 02451, USA) was used (250-1700 nm). Measurements with this instrument were taken with 1 nm resolution at 8° angle of incidence and used NIST-calibrated Spectralon (Labsphere, North Sutton, NH 03260, USA) as a reference. Spectra were also collected at room temperature in the mid- to long-wave infrared (MWIR-LWIR) with a PerkinElmer Spectrum 100 FT-IR integrating-sphere spectrometer (4.2-13.7 μm). This instrument provided spectra with 2 cm^{-1} resolution at normal illumination and used diffuse gold as a reference. MWIR-LWIR spectra were averaged over at least 25 scans to lessen the presence of atmospheric absorption. Owing to the integrating-sphere geometry in these commercial instruments, these spectra represent the total-integrated diffuse reflectance of the materials at each wavelength.

2.3. Temperature-dependent diffuse reflectance spectroscopy – near- to short-wave infrared (NIR-SWIR)

Temperature-dependent diffuse reflectance measurements were achieved on the NZ monolith in air using supercontinuum laser illumination and CO_2 laser heating (Fig. 21) [4]. There are a few important distinctions between these temperature-dependent diffuse reflectance measurements and the room-temperature, total-integrated diffuse reflectance spectra collected with commercial instrumentation.

In the temperature-dependent diffuse reflectance measurements, the material was illuminated by supercontinuum laser light at a 10° angle of incidence and scattered light was collected over a solid angle about the specular reflection direction (Fig. 21). Conversely, in the room-temperature diffuse reflectance measurements the material was illuminated with a 8° angle of incidence and an integrating-sphere collected light from all solid angles except that directly about the illumination direction. These differing approaches towards diffuse reflectance measurement should be equivalent, provided that the material being characterized has similar scattering characteristics to the reference material. In this work, NIST-calibrated Spectralon was used as a reference for the angularly-limited, temperature-dependent diffuse reflectance measurements.

The optical characteristics of the supercontinuum laser and the manner in which scattered light was analyzed also make the temperature-dependent diffuse reflectance measurements somewhat unconventional. The supercontinuum source is a high-power, broadband laser and light scattered from the material was analyzed with a spatially-resolved grating spectrometer (Fig. 21). Consequently, diffuse reflectance spectra can be simultaneously collected over the full wavelength range of the grating spectrometer. By comparison, integrating-sphere spectrometers typically use lamp illumination sources and incrementally scan through a wavelength range of interest using monochromators. It is the ability to accurately direct the supercontinuum laser beam, as well as its high optical intensity and spectral breadth that make this source particularly useful for temperature-dependent diffuse reflectance measurements.

An important geometrical consideration is the relative positions and spot sizes of the supercontinuum and CO_2 lasers. A LWIR camera was used to ensure concentricity of the supercontinuum and CO_2 laser hot spots (Fig. 21), which were nearly the same diameter (~2 mm). The LWIR camera was also used for pyrometric sample surface temperature determination (Section 6.2). To determine the so-called viewing area of the fiber-coupled grating spectrometer, a fiber-coupled diode laser (1310 nm) was projected through the collection optics and onto the sample surface. This projected spot size was significantly larger than the supercontinuum/CO_2 hot spots, therefore temperature-dependent diffuse reflectance spectra were collected from the CO_2 laser heated region as a whole. Reported temperatures for each spectrum represent a full-width at tenth-maximum (FWTM) average over the heated zone.

Table 4 shows the specifications for the instrumentation used in measuring the temperature-dependent diffuse reflectance spectra.

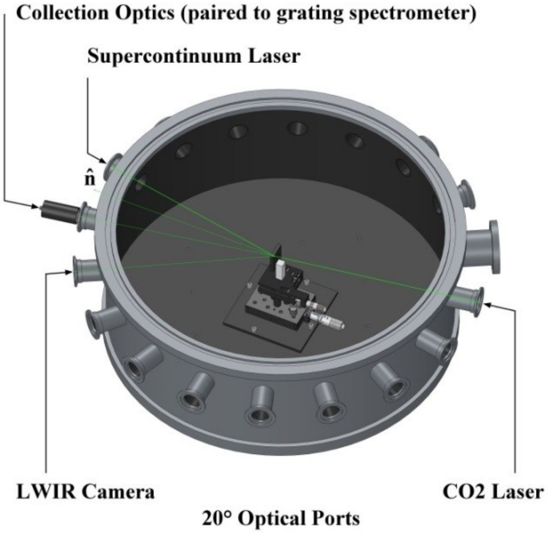

Fig. 21. Solid model of the black-coated optical chamber used for temperature-dependent diffuse reflectance spectroscopy showing the orientations of the various laser sources and instrumentation relative to the sample surface normal $\hat{n}$. Colors used are for illustration purposes only and are not meant to represent the wavelengths of the various laser sources.

Table 4. Specifications for the various instrumentation used in the temperature-dependent diffuse reflectance measurements.

Instrument	Model	Spectral Range	Additional Comments
Supercontinuum laser	SuperK EXTREME RED 80 MHz VIS (NTK Photonics, Denmark)	400-2400 nm	Propagated through 900 nm long pass filter
CO_2 laser	Firestar (SYNRAD, Mukilteo, WA 98275, USA)	10.6 µm	Tunable, 0-40 Watt nominal
Grating spectrometer	EPP2000-NIR-InGaAs (StellarNet, Tampa, FL 33626, USA)	970-1700 nm	25 µm slit with 1.25 nm resolution, 50 ms detector integration time and 100 scans to average
LWIR camera	Thermovision 900 (Agema, Sweden)	4.2-13.7 µm	None

3. Results and analysis

3.1. Room-temperature materials characterization

3.1.1. Ambient X-ray diffraction (XRD)

In Fig. 22, a direct comparison between phase content in the as-received $Nd_2Zr_2O_7$ powder and the as-sprayed NZ coating is shown. The as-received $Nd_2Zr_2O_7$ powder is found to be in the pyrochlore crystal structure, whereas the as-sprayed NZ coating has predominantly the defect fluorite crystal structure. These phases are distinguishable in XRD measurements by the presence of super-reflections in the diffraction pattern of the pyrochlore crystal structure and a lack thereof in that of the defect fluorite crystal structure. Super-reflections in the diffraction pattern of the pyrochlore crystal structure result from ordering of cations (RE^{3+} and Zr^{4+}) and anion vacancies (O^{2-}) in the lattice. In the defect fluorite crystal structure, cations and anion vacancies are more or less randomly distributed among the available sites. The difference in breadth and position of the diffraction peaks corresponding to these two phases should be noted. The diffraction peaks corresponding to the defect fluorite phase are significantly broadened and shifted relative to those of the pyrochlore phase – this effect is particularly evident at large values of 2θ. The significant breadth and shift of diffraction peaks corresponding to the defect fluorite phase may be due to strain in the material as a result of the size differential between the Nd^{3+} and Zr^{4+} ions and their random distributions.

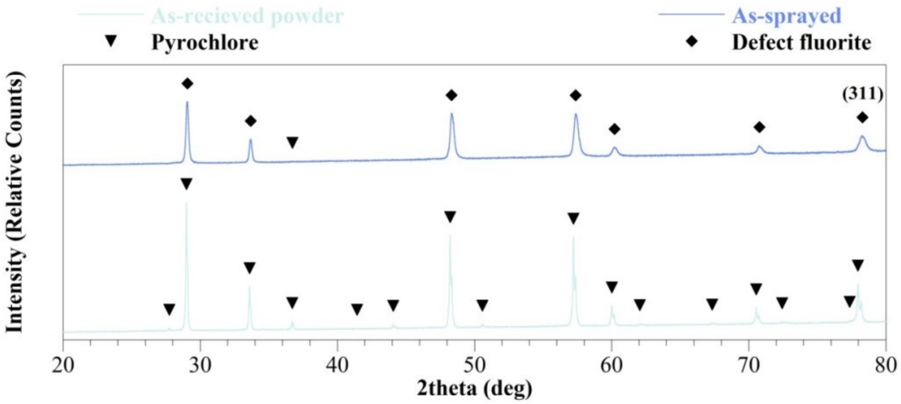

Fig. 22. X-ray diffraction patterns of the as-received $Nd_2Zr_2O_7$ powder and the as-sprayed neodymium zirconate (NZ) coating showing locations of diffraction peaks associated with the pyrochlore and defect fluorite crystal structures. The top scan corresponds to the as-sprayed NZ coating having predominantly the defect fluorite crystal structure and the bottom scan relates to the as-received $Nd_2Zr_2O_7$ powder in the pyrochlore crystal structure.

Based on the results shown in Fig. 22 and on the phase diagram of the $xNdO_{1.5}$-$(1-x)ZrO_2$ system, the as-received $Nd_2Zr_2O_7$ powder is likely near-stoichiometric due to the existence of the pyrochlore phase as only a line compound below 500 K at x = 0.5 [5]. Predictions of composition based on the phase content of a material depend on thermodynamic equilibrium being achieved. This is a reasonable assumption for the as-received $Nd_2Zr_2O_7$ powder due to the solid-state processing methods used, which requires sintering operations at very high temperatures for extended periods of time. The compositional nature of the as-sprayed NZ coating is much more difficult to predict, as the defect fluorite phase is not observed on the equilibrium phase diagram below ~1500 K for all compositions. It has been shown however that rare earth zirconate powders are susceptible to evaporation of rare earth content during plasma spraying [6], which would represent a compositional shift on the phase diagram towards the ZrO_2 axis. The as-sprayed NZ coating exists as a non-equilibrium phase under these APS deposition conditions, and may be subject to phase transformations at elevated temperatures.

3.1.2. Integrating-sphere diffuse reflectance spectroscopy

In Fig. 23 we compare the room-temperature optical behaviors of NZ in various physical forms. The $xNdO_{1.5}$-$(1-x)ZrO_2$ phase diagram shows stability of the pyrochlore phase to at least 2500 K, and this implies that the sintered pellet (1973 K, 4 h in air) has likely retained the crystal structure of the as-received $Nd_2Zr_2O_7$ powder (i.e. pyrochlore). A multitude of sharp absorptions are observed in the total-integrated diffuse reflectance spectra of the sintered pellet from the visible to the SWIR (400-1700 nm). This is to be expected based on the complete energy level diagram of the Nd^{3+} ion in LaF_3 [7-9]. These sharp absorptions are significantly blended in the as-sprayed NZ coating and this may be related to a non-uniform coordination environment for the Nd^{3+} ion and strain in the non-equilibrium defect fluorite phase. Interestingly, absorbance is quite high in the UV-Vis from 250-400 nm for both phases, despite a lack of many Nd^{3+} energy levels for valence band electronic transitions in this spectral region [7-9]. It is reasonable to assume that absorption in this spectral region is dominated by the promotion of electrons directly across the band gap. The basis for this assumption is found in previous reports [10-12], that provide values for the room-temperature direct band gap of NZ ranging from 2.67 to 4.00 eV, respectively. In these reports the direct band gap of pyrochlore NZ (4.00 eV, [10]) was calculated from first-principles and that of defect fluorite NZ (3.22 and 2.67 eV, [11,12]) was empirically-determined. The spectra reported in Fig. 23 qualitatively agree with these findings, as the direct band gap edge appears to shift to lower energy (i.e. longer wavelength) for the as-sprayed NZ coating (defect fluorite) relative to the sintered pellet (pyrochlore).

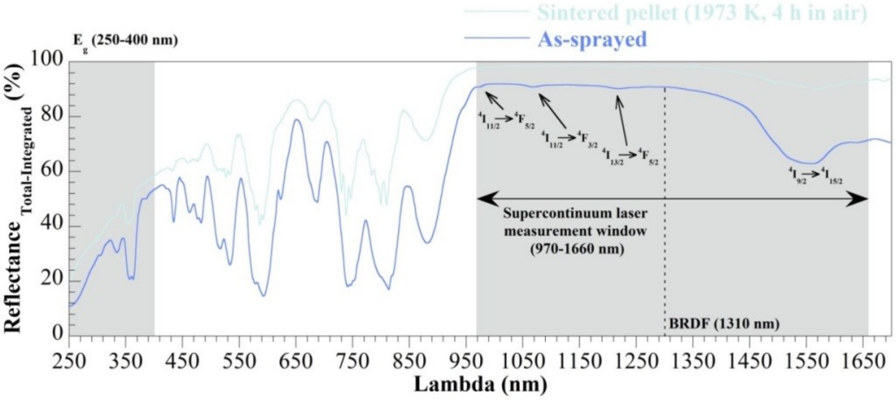

Fig. 23. A room-temperature comparison of the total-integrated diffuse reflectance spectra (8° angle of incidence) for physical forms of neodymium zirconate (NZ) having the pyrochlore (sintered pellet) and defect fluorite (as-sprayed coating) crystal structures. Several interesting structure-optical property relationships are noted, including a band gap shift to lower energy (longer wavelengths) for the as-sprayed NZ coating (defect fluorite) relative to the sintered pellet (pyrochlore).

3.1.3. Bidirectional reflectance distribution function (BRDF)

The NZ monolith was synthesized by heat treatment of the as-sprayed coating at 1073 K for 12 h. No significant structural change was observed in ambient XRD measurements for the NZ monolith relative to the as-sprayed coating, i.e. the non-equilibrium defect fluorite crystal structure was retained in the monolith. Temperature-dependent, diffuse reflectance measurements were made with the supercontinuum laser in the wavelength range 970-1660 nm. Owing to the use of NIST-calibrated Spectralon as a reference material in these measurements, the overall technique requires that the scattering characteristics of the NZ monolith must be approximately Lambertian in this wavelength range. This was determined to be true to a reasonable extent by measurement of the in-plane BRDF of the NZ monolith at room-temperature with a 1310 nm diode laser [13]. An appropriate choice of spectral location for this type of measurement is in a region where valence band electronic transitions in the Nd^{3+} ion do not contribute significantly to the optical behaviors of the material (Fig. 23 and [7-9]).

3.2. Temperature-dependent materials characterization

3.2.1. Physics-based modeling of optical properties

It is likely that high-temperature absorptive loss in the NZ monolith is dominated by free-carrier effects at many wavelengths (including 1310 nm) in the NIR-SWIR spectral region of our measurements [14]. This statement excludes spectral locations with the presence of absorption due to valence band electronic transitions in the Nd^{3+} ion. Wavelengths corresponding to the ${}^4I_{11/2}\rightarrow{}^4F_{5/2}$, ${}^4I_{11/2}\rightarrow{}^4F_{3/2}$, ${}^4I_{13/2}\rightarrow{}^4F_{5/2}$ and ${}^4I_{9/2}\rightarrow{}^4I_{15/2}$ absorption bands are therefore excluded from this development since they include valence band electronic transitions (Fig. 23). A physics-based model for the frequency v and temperature T dependence of the total-integrated diffuse reflectance $R(v,T)_{Total-Integrated}$ as a function of conduction band free electron concentration $N_f(T)$ can be used to understand the impact of free carriers on the measurements reported here. The constituent models presented in the following discussion can be found in Refs. 14-18.

The overall optical behavior of the materials studied here depend directly on scattering from elements of the microstructure and a starting point for describing this scattering is the widely-used Kubelka-Munk formulation. We choose to begin with an unmodified, two-flux, Kubelka-Munk model for diffuse radiation transfer in a free-standing film of thickness d [15]. For this film $R(v,T)_{Total-Integrated}$ can be written as follows:

$$R(v,T)_{Total-Integrated} = \frac{\frac{D}{B}(v,T)\,(-exp(-2\beta(v,T)d)+1)}{-\frac{D}{B}(v,T)^2\,exp(-2\beta(v,T)d)+1} \quad (1)$$

where $\frac{D}{B}(v,T)$ and $\beta(v,T)$ are ultimately functions of the Kubelka-Munk absorption $\beta_{abs}(v,T)$ and back-scattering $\beta_{back\,sca}(v,T)$ coefficients

$$\frac{D}{B}(v,T) = \frac{\beta_{ext}(v,T) - \beta(v,T)}{\beta_{back\,sca}(v,T)} \quad (2)$$

$$\beta(v,T) = \sqrt{\beta_{ext}(v,T)^2 - \beta_{back\,sca}(v,T)^2} \quad (3)$$

with

$$\beta_{ext}(v,T) = \beta_{abs}(v,T) + \beta_{back\,sca}(v,T) \quad (4)$$

Eqs. 5 and 6 contain the Mie absorption $C_{abs}(v,T)$ and scattering $C_{sca}(v,T)$ cross sections [16,17]. Multiplication of $C_{abs}(v,T)$ and $\frac{C_{sca}(v,T)}{2}$ by the number density of absorbers ρ_{abs} (i.e. NZ splats) and scatterers ρ_{sca}(i.e. pores) provides expressions for $\beta_{abs}(v,T)$ and $\beta_{back\,sca}(v,T)$.

$$\beta_{abs}(v,T) = \rho_{abs}C_{abs}(v,T) \quad (5)$$

$$\beta_{back\,sca}(v,T) = \frac{\rho_{sca}C_{sca}(v,T)}{2} \quad (6)$$

The assumption that scattering is dominated by the presence of porosity in the NZ deposit is supported by the relative transparency of dense NZ ceramics fabricated as solid-state laser materials [19]. In Eq. 6, we have assumed that the single-scatter event is spatially-isotropic, meaning that one half of the total scattered light is contained the back-hemisphere. In this work, the calculation of $C_{abs}(v,T)$ and $C_{sca}(v,T)$ using Mie theory necessarily assumed spherical splats and pores (monodisperse), which is a simplified representation of the complex microstructure of thermally-sprayed deposits [20]. A spherical representation of the splats and pores may however be a reasonable representation of a thermally-sprayed deposit under certain spray conditions (e.g. low plasma torch power for a highly-refractory feedstock material). In addition, temperature-dependent diffuse reflectance spectra were collected with collimated laser light, whereas the source term in the unmodified two-flux Kubelka-Munk model is diffuse. Since the aim with this modeling effort is to consider the conditions under which free-carrier absorption may or may not be a dominant loss mechanism for NZ in the NIR-SWIR, these differences are not of primary importance. The assumptions in the model simplify the overall problem. For example, using a spherical geometry for the NZ particles and pores allows for ready determination of physically-reasonable values for ρ_{abs} and ρ_{sca} from packing theory. It has been shown that the value of the packing fraction η is 0.64 for monodisperse spheres in random close packing [21]. We have developed a simple physical model for a plasma-sprayed deposit using $\eta = 0.64$. A monodisperse spherical splat diameter of 44 µm was chosen based on the sizing (-325 mesh) of the as-received $Nd_2Zr_2O_7$ powder. The remaining free space in the randomly-close-packed deposit was distributed among monodisperse spherical pores with a diameter of 10 µm. It is not uncommon for plasma-sprayed deposits to consist of globular porosity of this size with similar dimensions spatially [20].

To obtain $C_{abs}(v,T)$ and $C_{sca}(v,T)$ using Mie theory we need to relate the real $n(v,T)$ and imaginary $k(v,T)$ components of the complex index of refraction to $N_f(T)$. Expressions for $N_f(T)$ will be based on the assumed behavior of NZ as a donor-doped (i.e. extrinsic) semiconductor [14,18]. The complex index of refraction is given by:

$$n(v,T) = \sqrt{\frac{1}{2}\left(\sqrt{\epsilon_1(v,T)^2 + \epsilon_2(v,T)^2} + \varepsilon_1(v,T)\right)} \quad (7)$$

$$k(v,T) = \frac{\varepsilon_2(v,T)}{2n(v,T)} \quad (8)$$

where

$$\epsilon_1(v,T) = 2.11^2 - \frac{v_1(T)^2}{v^2 + v_2(T)^2} \quad (9)$$

$$\epsilon_2(v,T) = \frac{v_2(T)}{v}\frac{v_1(T)^2}{v^2 + v_2(T)^2} \quad (10)$$

$$v_1(T) = \sqrt{\frac{e^2 N_f(T)}{4\pi^2 \epsilon_0 m_{e_{eff}} m_e}} \quad (11)$$

$$v_2(T) = \frac{2\pi\epsilon_0 v_1(T)^2}{\sigma_0(T)} = \frac{2\pi\epsilon_0 v_1(T)^2}{|e|N_f(T)\mu_0} \quad (12)$$

In Eqs. 9-12 $v_1(T)$, $v_2(T)$, $\epsilon_1(v,T)$ and $\epsilon_2(v,T)$ are the Drude-model plasma and damping frequency, and the real and imaginary components of the complex relative permittivity, respectively. The constants e, m_e and ε_0 are the electron charge and mass, and the free space permittivity. The parameters $m_{e_{eff}}$, μ_0 and σ_0 are the effective mass and DC mobility of the conduction band electron, and the DC electrical conductivity, respectively. Here we have made use of the measured value 2.11 for the real component of the complex index of refraction for NZ at $v \gg v_1 \gg v_2$ [22].

In Eq. 13 the direct band gap at 0 K, E_{g_0}, can be calculated with knowledge of the room-temperature direct band gap [10-12] and the Debye temperature θ_D for NZ [23]. With E_{g_0} and Boltzmann's constant k_B, the direct band gap $E_g(T)$ is then determined by Eq. 13. The Fermi energy $E_f(T)$ can be determined computationally by Eq. 14 using a donor concentration N_D with associated energy level $E_d(T)$. Eq. 15 is then used to calculate $N_f(T)$. The parameters $m_{e_{eff}}$, $m_{h_{eff}}$ (effective mass of the valence band hole) and μ_0 can be bounded by values for common semiconductor materials, and in this work we have used order of magnitude values provided for ZnO in Ref. 14. Here we have used a temperature-independent μ_0, although electron mobility typically decreases with temperature due to increased electron-phonon interaction [14].

$$E_g(T) = E_{g_0} - \frac{(5 * 10^{-4})T^2}{T + \theta_D} \quad (13)$$

$$(4.84 * 10^{21}) {m_{e_{eff}}}^{3/2} T^{3/2}\, exp\left(\frac{-(E_g(T) - E_f(T))}{k_B T}\right) = \frac{N_D}{1 + 2\, exp\left(\frac{E_f(T) - E_d(T)}{k_B T}\right)} + (4.84 * 10^{21}) {m_{h_{eff}}}^{3/2} T^{3/2}\, exp\left(\frac{-E_f(T)}{k_B T}\right) \quad (14)$$

$$N_f(T) = \frac{N_D}{1 + 2\, exp\left(\frac{E_f(T) - E_d(T)}{k_B T}\right)} + (4.84 * 10^{21}) {m_{h_{eff}}}^{3/2} T^{3/2}\, exp\left(\frac{-E_f(T)}{k_B T}\right) \quad (15)$$

From Eqs. 1-15, we can determine $R(v,T)_{Total-Integrated}$ of NZ with knowledge of only $N_f(T)$ or $\sigma_0(T)$. It should be noted that measurements of $\sigma_0(T)$ for defect fluorite NZ are not reported and that published results for pyrochlore NZ may be complicated by contributions from ionic conductivity [24-25]. For example, Chapman *et al.* [24] and Guillou *et al.* [25] considered sintered pellets of pyrochlore NZ. Since the physical and structural form for the material studied in this work was defect fluorite NZ, values for various material properties likely differ. For these reasons we have focused on theoretical considerations for $N_f(T)$ based on NZ being an extrinsic semiconductor.

3.2.2. Diffuse reflectance spectroscopy – near- to short-wave infrared (NIR-SWIR)

In Fig. 24, the temperature-dependent diffuse reflectance spectra are shown for the NZ monolith, along with the total-integrated diffuse reflectance measured at room temperature for comparison. Agreement between the total-integrated diffuse reflectance measured at room temperature and the angularly-limited diffuse reflectance measured with the supercontinuum laser is quite good at the lowest achievable sample surface temperature (390 K). The absorption bands measured with the integrating-sphere spectrometer have been reproduced with the supercontinuum laser, and disagreement in spectral locations where valence band electronic transitions in the Nd^{3+} ion do not contribute significantly is seen to be on the order of a few percent. With heating up to 1240 K, we observe significant strengthening of the absorptions which originate from the $^4I_{11/2}$ level ($^4I_{11/2}\rightarrow{}^4F_{5/2}$, $^4I_{11/2}\rightarrow{}^4F_{3/2}$). This is due to thermalization of the $^4I_{11/2}$ level, and is known to occur with temperature for the Nd^{3+} ion in yttrium aluminum garnet (YAG) host [26,27]. Accordingly, absorption bands which originate from the $^4I_{11/2}$ level are commonly referred to as “hot bands”. Absorptions which originate from the $^4I_{9/2}$ (ground state) and the $^4I_{13/2}$ levels show less of a temperature dependence, which would suggest their populations are more or less thermally-stable in this temperature range. Of particular interest from 390-1240 K is a reflectance reduction with increasing temperature in spectral locations where valence band electronic transitions in the Nd^{3+} ion (e.g., 1310 nm) do not contribute significantly. Above 1240 K, observations of further temperature dependencies are concealed by the presence of a measurable thermal emission component at all wavelengths. In fact, the measured diffuse reflectance exceeds one on the long-wavelength-side of the spectral measurement range at temperatures above 1510 K. The presence of the diode pump laser for the supercontinuum source centered at 1064 nm and the accuracy of the angularly-limited diffuse reflectance measurements obtained with the supercontinuum laser are discussed in Section 6.1.

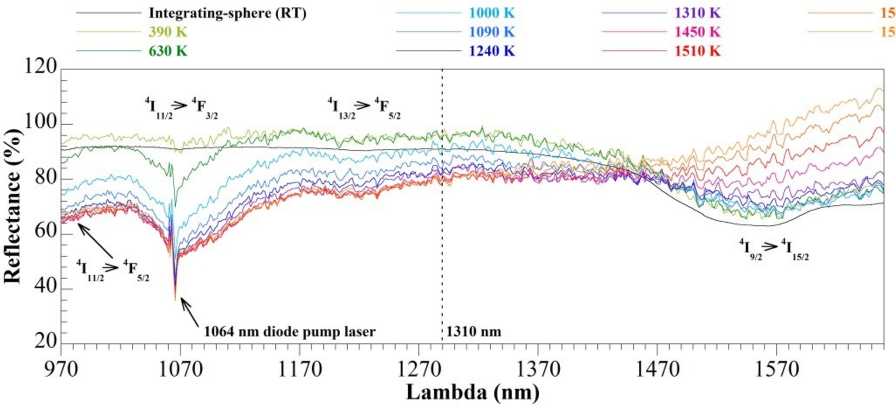

Fig. 24. Diffuse reflectance (10° angle of incidence) spectroscopy of the neodymium zirconate (NZ) monolith has revealed several interesting temperature dependencies. Most notable is the reflectance reduction with increasing temperature at spectral locations where valence band electronic transitions in the Nd^{3+} ion do not contribute significantly (e.g., 1310 nm) and the emergence of a broadband thermal emission component at high temperature.

In order to account for the thermal emission component in the diffuse reflectance measurements, a set of strictly thermal emission measurements were collected for the NZ monolith. These measurements were performed with CO_2 laser heating only (no supercontinuum laser illumination) and used the same collection optics as the diffuse reflectance measurements. This dataset was used to fit the measured thermal emission intensity as a function temperature at each spectral location. A 4th-order polynomial was found to be a reasonable functional fit to the thermal emission intensity as a function of temperature at each spectral location. We have used these polynomial fits to remove the thermal emission component from the diffuse reflectance measurements. The results are shown in Fig. 25, where the corrected diffuse reflectance is presented for the NZ monolith.

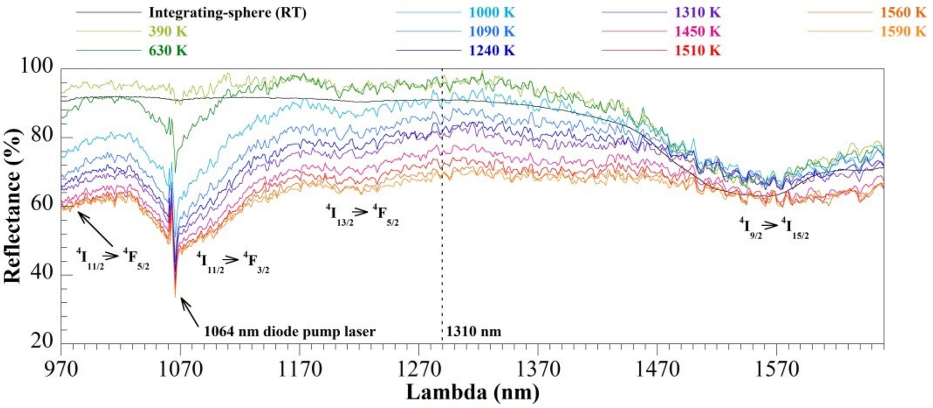

Fig. 25. The corrected diffuse reflectance of the neodymium zirconate (NZ) monolith provides further insight towards optical property temperature dependencies in the material. The reduction of the reflectance in spectral locations where valence band electronic transitions in the Nd^{3+} ion do not contribute significantly (1310 nm) is most notable as this may be related to free-carrier absorption.

It is now apparent that the "hot band" electronic transitions which originate from the $^4I_{11/2}$ level have continued to grow in strength above 1240 K up to highest achievable sample surface temperature (1590 K). Conversely, electronic transitions which originate from the $^4I_{9/2}$ (ground state) and $^4I_{13/2}$ levels display little dependence on temperature above 1240 K. In spectral regions away from these valence band electronic transitions in the Nd^{3+} ion, a relatively uniform reduction of the reflectance occurs with increasing temperature.

3.2.3. Analysis of diffuse reflectance spectra

Gupta *et al.* have provided first-principles calculations of the electronic band structure of NZ in the ideal state as well as in several defected states [11]. They have studied the effect of neutral oxygen vacancies at the crystallographic site nearest-neighbor to the Nd^{3+} ion and reported a shift in the room-temperature direct band gap from 3.22 (ideal) to 2.80 eV (defected). Also of significance is the presence of a populated donor state within the band gap of the material at an energy level which resides 1.18 eV below the conduction band. Figure 26 shows $R(v,T)_{Total-Integrated}$ at 1310 nm for the defected electronic band structure of NZ described by Gupta *et al.* [11]. Calculations for $N_D = 0$ and $N_D = 5 * 10^{26}$ are shown which represent the intrinsic and extrinsic semiconductor behaviors of the material, respectively. Also included for comparison are the reflectance values from our measurements at 1310 nm.

There are several important observations to make using the modeling results. Among these are the dependence of the "break" temperature and the strength of free-carrier absorption on the semiconductor behavior of NZ (Fig. 26). By "break" temperature what is meant is the point at which the second derivative of $R(v,T)_{Total-Integrated}$ goes through an inflection point. We note that the break temperature deviates by 1100 K between the extrinsic $(693\,K, N_D = 5 * 10^{26})$ and intrinsic $(1793\,K, N_D = 0)$ behaviors. From inspection of Fig. 26, it is clear that the intrinsic behavior of NZ does not describe our experimental observations up to ~1593 K, and it appears that the extrinsic behavior of NZ is responsible for a significant reduction of $R(v,T)_{Total-Integrated}$ up to ~1593 K in this spectral region in highly-scattering media. It should also be stated that the donor concentration of $N_D = 5 * 10^{26}$ used to achieve semi-quantitative agreement is physically reasonable, as it is orders of magnitude less than the theoretical number of Nd^{3+} ions in NZ [19].

The modeling effort also provides predictive capability for the upper temperature limit of the extrinsic behavior of NZ. Above 1693 K, electronic transitions from the donor energy level to the conduction band have saturated, and the intrinsic behavior of the material begins to dominate. This saturation behavior is of course predicated on the lack of donor energy levels at more than 1.18 eV below the conduction band. By tailoring spray parameters to intentionally introduce defect energy levels, a material could be produced that might extend the extrinsic behavior of NZ to temperatures above 1693 K.

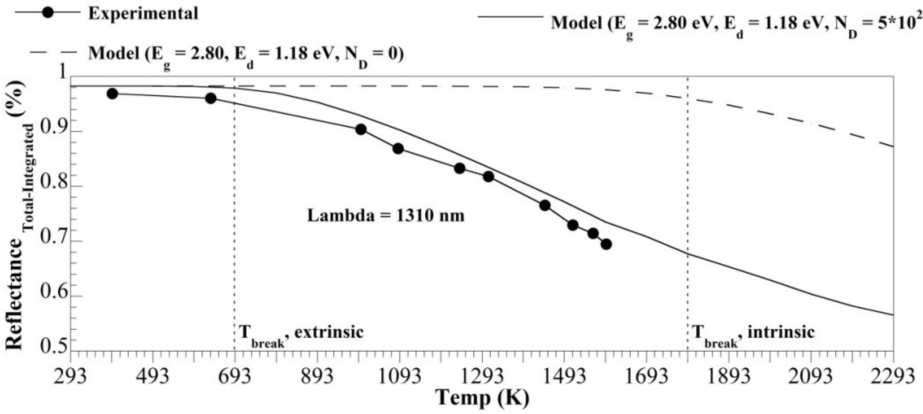

Fig. 26. Physics-based modeling of the temperature-dependent, total-integrated reflectance of neodymium zirconate (NZ) at 1310 nm using the defected electronic band structure for NZ described in Ref. 11.

3.2.4. Non-ambient X-ray diffraction (XRD)

We have used non-ambient XRD to investigate the significant reduction reflectance between 1310 and 1450 K (Fig. 25). It should be noted that the NZ monolith is kinetically-stable (on the order of an hour) in the non-equilibrium defect fluorite crystal structure up to at least 1453 K based on the phase content in non-ambient XRD measurements. The significant breadth of the diffraction peak corresponding to the (311) crystallographic plane in the defect fluorite phase makes this peak most suitable for analysis of isostructural changes with temperature (Fig. 22). In Fig. 27, the temperature dependence of the (311) diffraction peak full-width half-max (FWHM) is presented for the NZ monolith. From room temperature up to 1293 K a slight reduction in the FWHM of the (311) diffraction peak is observed. This is in contrast to the thermal broadening of diffraction peaks one would expect for a thermodynamically-stable material [28]. Above 1293 K, an irreversible reduction in the FWHM occurs which may be related to strain relief in the material. Limitations on the high-temperature chamber for the non-ambient XRD prevented investigation beyond 1453 K. While it is not possible to determine if strain relief at 1293 K is associated with a progression towards thermodynamic equilibrium, it does appear to correspond with the significant reduction of reflectance between 1310 and 1450 K.

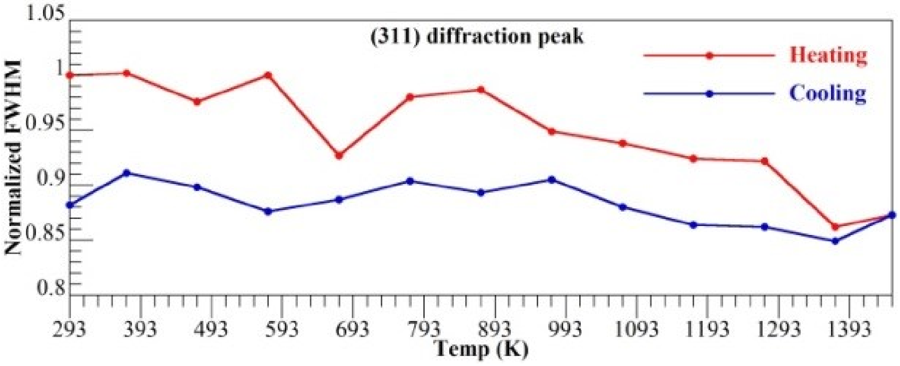

Fig. 27. Non-ambient XRD measurement of the (311) diffraction peak full-width half-max (FWHM) is presented for the neodymium zirconate (NZ) monolith. This material is in the non-equilibrium defect fluorite crystal structure at room temperature, and shows a potential onset of progression towards thermodynamic equilibrium at 1293 K, although it is kinetically-stable to at least 1453 K (on the order of an hour).

4. Discussion

If we consider the multitude of possible defect-types in these zirconate materials (e.g., loss of cation/anion-vacancy ordering, cation/anion vacancies) and the coating deposition method at hand, it is conceivable that plasma-sprayed defect fluorite NZ has a significant density of donor states within the band gap that can lead to increased free-carrier absorption at lower temperatures. This work represents a rationale for a more detailed investigation of the non-equilibrium defect fluorite rare earth zirconates. Previous work has focused on optimization of spray parameters for retention of the pyrochlore phase [6]. We suggest retention of the defect fluorite phase may be preferable from a radiation transfer perspective in certain applications. Detailed investigations should include examination of the high-temperature stability range of the non-equilibrium defect fluorite phases, temperature-dependent band gap determinations [29] and electrical property measurements at elevated temperatures. It is important in future high-temperature electrical measurements that the contributions to properties such as conductivity due to electrons, holes and ions are separable by way of appropriate measurement techniques [30]. With this collective information, it should be possible to complete physics-based models for free-carrier absorption in the defect fluorite rare earth zirconates and identify suitable applications within the range of stable temperatures.

5. Conclusion

Under certain spray conditions, the non-equilibrium defect fluorite phase may be retained in deposits of plasma-sprayed pyrochlore $Nd_2Zr_2O_7$. Diffuse reflectance spectroscopy, both at room and elevated temperatures, has provided evidence to support the notion that the defect fluorite phase may be preferable to the pyrochlore phase, particularly in applications where increased radiation transfer is of interest. Free-carrier absorption has been proposed as a dominant, broadband infrared absorption mechanism at high temperatures in these doped/stabilized cubic zirconias. The electronic band structure of the defect fluorite phase is altered relative to that of the pyrochlore phase for neodymium zirconate, and this may be beneficial for enhancing free-carrier absorption in the deposit. As illustrated in this work, an understanding of the materials paradigm for the rare earth zirconates as it relates to optical properties will be critical in the design of next-generation thermal barrier coatings.

6. Supplemental material

6.1. Supercontinuum laser stability and accuracy of reported spectra

The particular supercontinuum laser source used in this work (Table 4) consists of a 1064 nm diode laser pumped into a photonic crystal fiber. As such, a broadband laser source is obtained from a spectrally-pure pump laser (Fig. 28). In Fig. 28, the NIR-SWIR (970-1700 nm) stability of the supercontinuum source is investigated by collection of diffusely-reflected laser light from NIST-calibrated Spectralon as a function of time. A relatively intense peak is observed at 1064 nm as a result of diode pump laser power transmission through the photonic crystal fiber. This feature appears in our temperature-dependent diffuse reflectance measurements (Figs. 24 and 25). From Fig. 28, it is qualitatively apparent that the supercontinuum laser source begins to thermally-equilibrate after a period of 1 h from initial emission.

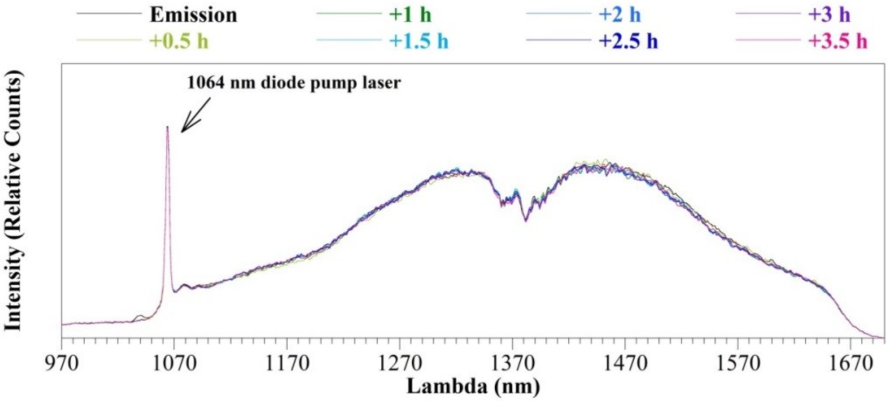

Fig. 28. Collection of diffusely-reflected laser light from NIST-calibrated Spectralon as a function of time provides a qualitative measure of the NIR-SWIR (970-1700 nm) stability of the supercontinuum source. The supercontinuum laser begins to thermally-equilibrate after 1 h from initial emission.

The stability of the supercontinuum laser is treated quantitatively in Fig. 29, where each subsequent spectrum (0.5 h increments) is divided by the spectrum obtained 1 h after initial emission. The measurement range of 970-1700 nm is further limited to 970-1660 nm by the lack of spectral response for the grating spectrometer detector (Table 4) from 1660-1700 nm. Fluctuations in measured intensity at each wavelength are on the order of a few percent. The average and standard deviations for these fluctuations over the useful measurement range of 970-1660 nm are presented in Table 5. Measurement of diffusely-reflected laser light from NIST-calibrated Spectralon after a source warm-up period of 1 h served as a reference spectrum for measurements on the NZ monolith. Accordingly, the data presented in Fig. 29 and Table 5 represent the accuracy of the spectra reported in Figs. 24 and 25.

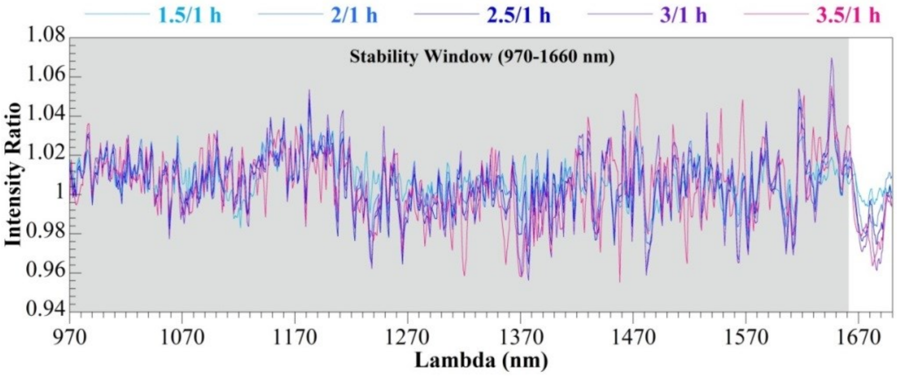

Fig. 29. The NIR-SWIR (970-1700 nm) stability of the supercontinuum laser is quantitatively treated by dividing each subsequent spectrum (0.5 increments) by the spectrum obtained 1 h after initial emission. A useful measurement range of 970-1660 nm is established by the lack of spectral response for the grating spectrometer detector (Table 4) from 1660-1700 nm.

Table 5. Statistical analysis of supercontinuum laser stability over the useful measurement range of 970-1660 nm.

	1.5/1 h	2/1 h	2.5/1 h	3/1 h	3.5/1 h
Average	1.0073	1.0080	1.0051	1.0057	1.0052
STD	0.0095	0.0127	0.0146	0.0165	0.0163

6.2. Band-averaged emissivity calculation for sample surface temperature correction

In Fig. 30 the room-temperature, total-integrated diffuse reflectance of the NZ monolith is presented for the MWIR-LWIR. Also provided is the spectral response function (SRF) of the LWIR camera (Table 4) used for pyrometric sample surface temperature determination. Of note is the high absorbance of the NZ monolith at the 10.6 μm spectral location, which motivated the choice of the CO_2 laser as a heating source. The NZ monolith is seen to be near-black-body over a large portion of the LWIR camera SRF.

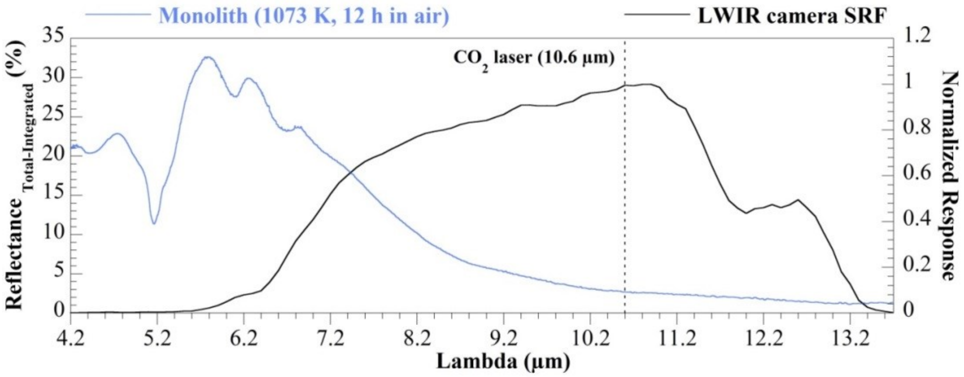

Fig. 30. The room-temperature, total-integrated diffuse reflectance (normal illumination) of the NZ monolith in the MWIR-LWIR has important implications. Beyond motivating the choice of CO_2 laser heating at the 10.6 μm spectral location, this measurement was used in calculating a band-averaged emissivity for the NZ monolith over the LWIR camera Spectral Response Function (SRF).

We calculated a band-averaged emissivity for the NZ monolith $E_{band-averaged_{NZ\ monolith}}$ over the LWIR camera SRF for correction of sample surface temperatures [4]:

$$E_{band-averaged_{NZ\ monolith}}(T)$$

$$= \frac{\int E_{NZ\ monolith}(\tilde{\nu}) SRF_{LWIR\ camera}(\tilde{\nu}) L_{BB}(\tilde{\nu}, T) d\tilde{\nu}}{\int SRF_{LWIR\ camera}(\tilde{\nu}) L_{BB}(\tilde{\nu}, T)\, d\tilde{\nu}} \quad (A1)$$

$$E_{NZ\ monolith}(\tilde{\nu}) = 1 - R_{NZ\ monolith}(\tilde{\nu}, \theta_i = 0) \quad (A2)$$

$$L_{BB}(\tilde{\nu}, T) = \frac{2h\tilde{\nu}^3 c^2}{\exp\left(\frac{hc\tilde{\nu}}{k_B T}\right) - 1} \quad (A3)$$

In Eq. A2, $E_{NZ\ monolith}(\tilde{\nu})$ is the spectral emittance of the NZ monolith and $R_{NZ\ monolith}(\tilde{\nu}, \theta_i = 0)$ is the total-integrated diffuse reflectance of the NZ monolith at normal illumination (Fig. 30). The blackbody spectral radiance $L_{BB}(\tilde{\nu}, T)$ is described by Eq. A3. $E_{band-averaged_{NZ\ monolith}}$was calculated from 293-1693 K in 100 K increments and an averaged value of 0.8873 was used for correction of sample surface temperatures. It is important to note that Eqs. A2 and A3 are a function of the spatial frequency $\tilde{\nu}$, as opposed to the temporal frequency ν used in Eqs 1-15. This procedure for calculating $E_{band-averaged_{NZ\ monolith}}$assumes optical opacity of the NZ monolith in the MWIR-LWIR, and a lack of temperature dependence for the optical constants of the material in this spectral region. The first assumption is supported by the thickness of the NZ monolith (~1 mm), and the second by temperature-dependent MWIR-LWIR emittance spectra measured in a separate facility [31].

References

1. H. Lehmann, D. Pitzer, G. Pracht, R. Vassen, D. Stöver, "Thermal Conductivity and Thermal Expansion Coefficients of the Lanthanum Rare-Earth-Element Zirconate System," Journal of the American Ceramic Society **86(8)**, 1338-1344 (2003).
2. J. Shunkwiler, Trans Tech, Inc., 5520 Adamstown Road, Adamstown, MD 21710, (2017).
3. L. Wang, J.E. Eldridge, S.M. Guo, "Thermal Radiation Properties of Plasma-Sprayed $Gd_2Zr_2O_7$ Thermal Barrier Coatings," Scripta Materialia **69**, 674-677 (2013).
4. M.C. Brupbacher, D. Zhang, W.M. Buchta, M.B. Airola, D.M. Brown, M.E. Thomas, J.B. Spicer, "Temperature-Dependent Diffuse Reflectance Spectroscopy of Plasma-Sprayed Cr-Doped α-Alumina using Supercontinuum Laser Illumination and CO_2 Laser Heating," Applied Optics, Under Review (2017).
5. C. Wang, M. Zinkevich, F. Aldinger, "Phase Diagrams and Thermodynamics of Rare-Earth-Doped Zirconia Ceramics," Pure and Applied Chemistry **79(10)**, 1731-1753 (2007).
6. G. Mauer, D. Sebold, R. Vaßen, D. Stöver, "Improving Atmospheric Plasma Spraying of Zirconate Thermal Barrier Coatings Based on Particle Diagnostics," Journal of Thermal Spray Technology **21(3-4)**, 363-371 (2012).
7. P.S. Peijzel, A. Meirjerink, R.T. Wegh, M.F. Reid, G.W. Burdick, "A Complete $4f^n$ Energy Level Diagram for All the Trivalent Rare Earth Ions," Journal of Solid State Chemistry **178**, 448-453 (2005).

8. W.T. Carnall, G.L. Goodman, K. Rajnak, R.S. Rana, "A Systematic Analysis of the Spectra of the Lanthanides Doped into Single Crystal LaF_3," Journal of Chemical Physics **90(7)**, 3343-3457 (1989).
9. W.T. Carnall, H. Crosswhite, H.M. Crosswhite, "Energy Level Structure and Transition Probabilities in the Spectra of the Trivalent Lanthanides in LaF_3," Argonne National Laboratory, 9700 Cass Avenue, Lemont, IL, 60439, (1977).
10. J. Feng, B. Xiao, C.L. Wan, Z.X. Qu, Z.C. Huang, J.C. Chen, R. Zhou, W. Pan, "Electronic Structure, Mechanical Properties and Thermal Conductivity of $Ln_2Zr_2O_7$ (Ln = La, Pr, Nd, Sm, Eu, and Gd) Pyrochlore," Acta Materialia **59**, 1742-1760 (2011).
11. S.K. Gupta, K. Sudarshan, P.S. Ghosh, A.P. Srivastava, S. Bevara, P.K. Pujari, R.M. Kadam, "Role of Various Defects in the Photoluminscence Characterisitics of Nanocrystalline $Nd_2Zr_2O_7$: An Investigation Through Spectroscopic and DFT Calculations," Journal of Materials Chemistry C **4**, 4988-5000 (2016).
12. M. Uno, A. Kosuga, M. Okui, K. Horisaka, H. Muta, K. Kurosaki, S. Yamanaka, "Photoelectrochemical Study of Lanthanide Zirconium Oxides, $Ln_2Zr_2O_7$ (Ln = La, Ce, Nd and Sm)," Journal of Alloys and Compounds **420**, 291-297 (2006).
13. A. M. Brown, D. V. Hahn, M. E. Thomas, D. M. Brown, J. Makowski, "Optical material characterization through BSDF measurement and analysis," in *Proceedings of SPIE* **7792**, 779211 (2010).
14. R.E. Hummel, *Electronic Properties of Materials*, 4th ed., (Springer, 2011).
15. P. Kubelka, F. Munk, "Ein Beitrag Zur Optik Der Farbanstriche," Zeitschrift Für Technische Physik **12**, 593-601 (1931).

16. C.F. Bohren, D.R. Huffman, *Absorption and Scattering of Light by Small Particles*, (Wiley Interscience, 1998).

17. J.-P. Schäfer, “Implementierung Und Anwendung Analytischer Und Numerischer Verfahren Zur Lösung Der Maxwellgleichungen Für Die Untersuchung Der Lichtausbreitung In Biologischem Gewebe,” Ph.D. Thesis, Universität Ulm, (2011).

18. G. Burns, *Solid State Physics*, (Academic Press, 1985).

19. T. Feng, D.R. Clarke, D. Jiang, J. Xia, J. Shi, “Neodymium Zirconate ($Nd_2Zr_2O_7$) Transparent Ceramics as a Solid State Laser Material,” Applied Physics Letters **98**, 151105 1-3 (2011).

20. C.-J. Li, A. Ohmori, “Relationship Between the Microstructure and Properties of Thermally Sprayed Deposits,” Journal of Thermal Spray Technology **11(3)**, 365-374 (2002).

21. J. G. Berryman, “Random Close Packing of Hard Spheres and Disks,” Physical Review A **27(2)**, 1053-1061 (1983).

22. A.K. Kuznetsov, É.K. Keler, “Zirconates of the Rare Earth Elements and Their Physiochemical Properties Communication 3. Some Principles of the Formation, Physiochemical and Technical Properties of the Zirconates,” Russian Chemical Bulletin **15(12)**, 2011-2016 (1966).

23. K. Shimamura, T. Arima, K. Idemitsu, Y. Inagaki, “Thermophysical Properties of Rare-Earth-Stabilized Zirconia and Zirconate Pyrochlores as Surrogates for Actinde-Doped Zirconia,” International Journal of Thermophysics **28**, 1074-1084 (2007).

24. R.A. Chapman, D.B. Meadowcroft, A.J. Walkden, "Some Properties of Zirconates and Stannates with the Pyrochlore Structure," Journal of Physics D: Applied Physics **3**, 307-319 (1970).
25. M. Guillou, J. Millet, M. Asquiedge, N. Busson, M. Jacquin, S. Palous, M. Pithon, A. Lecante, "Propriétés Électroniques A Haute Température Du Systéme Zircone-Oxyde De Néodyme," Revue Internationale Des Hautes Températures Et Des Réfractaires **4**, 273-280 (1967).
26. J. T. Verdeyen, *Laser Electronic*, 3rd ed., (Prentice Hall, 1995).
27. R.M. Springer, M.E. Thomas, "Transmittance Derived Line Width and Line Shift in Polycrystalline Nd:YAG," Applied Optics **55(31)**, C1-C8 (2016).
28. B.D. Cullity, S.R Stock, *Elements of X-ray Diffraction*, 3rd ed., (Prentice Hall, 2001).
29. J.-H. Park, R.N. Blumenthal, "High-Temperature Optical Absorption Measurement of Single-Crystal, Yttria-Stabilized Zirconia," Journal of the American Ceramic Society **71(11)**, C-462-C-463 (1988).
30. J.-H. Park, R.N. Blumenthal, "Electronic Transport in 8 Mole Percent Y_2O_3-ZrO_2," Journal of the Electrochemical Society **136(10)**, 2867-2876 (1989).
31. P.J. Bonzani Jr., E.H. Florczak, J.J. Scire Jr., J.R. Markham, "Improvement to a Bench Top Instrument for Measuring Spectral Emittance at High Temperatures," Review of Scientific Instruments **74(6)**, 3130-3136 (2003).

Chapter 5: Conclusion

While baseline materials characterizations such as X-ray diffraction and scanning electron microscopy were used to ensure adequate processing and interpret spectra, a large portion of the results presented in this dissertation were in the form of optical property measurements. The familiar integrating-sphere spectrometer was used extensively to make room-temperature diffuse reflectance measurements that provided a variety of information. Of particular significance, these diffuse reflectance spectra measured with commercial instrumentation served as room-temperature validation of those measured with an experimental technique demonstrated for the first time – temperature-dependent diffuse reflectance spectroscopy using supercontinuum laser illumination and CO_2 laser heating. This experimental technique was applied to both doped-metal-oxide systems (i.e. the transition-metal-doped aluminas and the rare earth zirconates), and was demonstrated in both the visible to near-infrared and the near-infrared to short-wave infrared spectral regions.

In Chapter 2, a procedure for producing monolithic doped metal oxides suitable for laser heating was presented. With the development of monolithic Cr-doped α-alumina, temperature-dependent supercontinuum laser diffuse reflectance spectroscopy was introduced and applied for the first time. Measurements were presented for monolithic Cr-doped α-alumina in the visible to near-infrared spectral region. These measurements provided previously unreported information regarding the thermally-activated splitting of the pump absorption band at high temperature and the thermal quenching of the fluorescence band at lower temperatures in monolithic Cr-doped α-alumina.

While each of these contributions has significance to a variety of applications, the strength of supercontinuum laser diffuse reflectance spectroscopy resides in the ability to simultaneously measure the temperature dependencies of both the pump absorption and fluorescence bands – a feature uncharacteristic of commercial integrating-sphere spectrometers with double-monochromator arrangements. With this collective information, Chapter 3 explored supercontinuum laser diffuse reflectance spectroscopy in conjunction with an extended Kubelka-Munk model for diffuse light propagation in highly-scattering and fluorescent media as a methodology for determining temperature-dependent quantum efficiency. The high-temperature applicability conditions of the extended Kubelka-Munk model were also considered.

In Chapter 4, temperature-dependent supercontinuum laser diffuse reflectance spectroscopy was reintroduced as it pertained to the near-infrared to short-wave infrared spectral region, and the technique was applied to monolithic, plasma-sprayed $Nd_2Zr_2O_7$ in this spectral region. In spectral locations away from regions affected by dopant-related absorption bands, reductions in reflectance were observed with increasing temperature. Interpretation of these measurements was provided by relating the standard Kubelka-Munk model for highly-scattering, non-fluorescent media to fundamental theories describing free carrier absorption. Modeling results suggested that under certain depositions conditions plasma-sprayed $Nd_2Zr_2O_7$ behaves like an extrinsic semiconductor. This result has implications for the design of next-generation thermal barrier coatings.

All of the monolithic doped metal oxides used in this work were derived from atmospheric plasma spray. This method essentially produced doped metal oxide samples that were chemically pure and could be used to obtain meaningful optical property information from spectroscopic measurements. Indeed, in the case of laser heating, optical-quality materials such as dense, sintered ceramics are undesirable since thermally-induced stresses can fracture these kinds of materials. Although many polycrystalline optical materials have application in coating form, it would be desirable to produce monolithic doped metal oxides suitable for laser heating by means other than thermal spray. Thermal spray facilities are not readily accessible in the research community when compared to traditional ceramic powder processing equipment, and thermal spray is often prohibitively inefficient when working with expensive rare earth dopants. Thus, future efforts to produce intentionally-porous, monolithic doped metal oxides by means other than thermal spray could extend the utility of the measurement techniques developed in this work.

Focusing on the optical measurement techniques themselves, a commercial integrating-sphere spectrometer could likely be retrofit with CO_2 laser heating to measure certain aspects of the temperature-dependent supercontinuum laser diffuse reflectance spectra. However, due to the double-monochromator arrangement typical of these instruments, optical properties in a spectral region of interest are determined by incrementally scanning through the desired wavelength range. This feature immediately excludes the ability to make measurements that contain fluorescent components. That these scans typically occur over a period on the order of minutes also has significant disadvantage. It may be desirable to study the optical properties of non-equilibrium phases at specific high-temperatures as a function of time. If the phase transformation to the equilibrium phase occurs on the time-scale of the integrating-sphere scan or less, there is no information to be gained in this regard with respect to commercial instrumentation. It may also be desirable to study the effect of additional extreme environmental conditions on optical properties. For instance, free-carrier absorption effects in oxygen-deficient doped metal oxides at high temperatures are likely dependent on O_2 partial pressure, and as a result also time. While it may be relatively trivial to retrofit a commercial-integrating sphere spectrometer with CO_2 laser heating, these instruments are certainly not equipped to operate in low O_2 partial pressure atmospheres. The facility developed in this work for temperature-dependent supercontinuum laser diffuse reflectance spectroscopy is capable of making measurements in low O_2 partial pressure atmospheres as a function of time.

Consideration to the range of physical forms applicable to supercontinuum laser diffuse reflectance spectroscopy must also be given. Commercial integrating-sphere spectrometers are typically limited to measurements on bulk samples and media appropriate for use in a cuvette (e.g., solutions, colloids, suspensions). Supercontinuum laser diffuse reflectance spectroscopy is applicable to these physical forms all well as others, including aerosols. With consideration to the physical forms relevant to supercontinuum laser diffuse reflectance spectroscopy, comments regarding the physical applicability of the technique are also appropriate. Supercontinuum laser diffuse reflectance spectroscopy is well equipped to make measurements on dynamic targets in the field, such as atmospheric aerosols.

Curriculum Vitae

Michael Collins Brupbacher was born in Baltimore, MD in 1988. He received his Bachelor of Mechanical Engineering from the University of Delaware in 2010. In 2011, he enrolled in the graduate program in Materials Science and Engineering at The Johns Hopkins University under advisement of Dr. James B. Spicer. He received his Master of Science in Engineering in May 2015, and defended his Ph.D. thesis in August 2017. Important publications and patents to date include:

Publications

1. M.C. Brupbacher, D. Zhang, W.M. Buchta, M.L Graybeal, Y.-R. Rhim, D.C. Nagle, J.B. Spicer, "Synthesis and characterization of binder-free Cr_3C_2 coatings on nickel-based alloys for molten fluoride salt corrosion resistance," Journal of Nuclear Materials **461**, 215-220 (2015).
2. M.C. Brupbacher, D. Zhang, W.M. Buchta, Y.-R. Rhim, D.C. Nagle, J.B. Spicer, "Post-treatment of plasma-sprayed Cr_2O_3 with methane-containing gas for conversion to binder-free Cr_3C_2," Journal of Thermal Spray Technology **24(8)**, 1513-1519 (2015).
3. M.C. Brupbacher, D. Zhang, W.M. Buchta, M.B. Airola, D.M. Brown, M.E. Thomas, J.B. Spicer, "Temperature-dependent diffuse reflectance spectroscopy of plasma-sprayed Cr-doped α-alumina using supercontinuum laser illumination and CO_2 laser heating," Applied Optics, Under Review (2017).

4. M.C. Brupbacher, D. Zhang, W.M. Buchta, M.B. Airola, D.M. Brown, M.E. Thomas, J.B. Spicer, "Supercontinuum laser diffuse reflectance spectroscopy in conjunction with extended Kubelka-Munk theory: a methodology for determination of temperature-dependent quantum efficiency in highly-scatter and fluorescent media," Applied Optics, In Preparation (2017).
5. M.C. Brupbacher, D. Zhang, W.M. Buchta, T.J. Montalbano, K.S. Caruso, M.B. Airola, D.M. Brown, M.E. Thomas, J.B. Spicer, "Determination of high-temperature, infrared spectral reflectance of plasma-sprayed $Nd_2Zr_2O_7$ and the implications for next-generation thermal barrier coatings design," Journal of Thermal Spray Technology, In Preparation (2017).

Patents

1. M.C. Brupbacher, D. Zhang, D.C. Nagle, "Method for forming binder-free refractory carbide, nitride and boride coatings with a controlled porosity," U.S. Provisional Patent Application No. 62/076,073.
2. M.C. Brupbacher, D. Zhang, D.C. Nagle, "Method for forming functionally-filled refractory carbide, nitride and boride coatings," U.S. Provisional Patent Application No. 62/192,668.
3. M.C. Brupbacher, D. Zhang, W.M. Buchta, "High-temperature, oxidation-resistant silicide coatings for industrial-scale structures in oxidizing atmospheres," U.S. Provisional Patent Application No. 62/458,659.

4. D. Zhang, M.C. Brupbacher, K.S. Caruso, W.M. Buchta, “Ceramic materials and coatings with high broad-band spectral reflectance,” U.S. Provisional Patent Application No. 62/458,652.
5. J. Erlebacher, I. McCue, B. Gaskey, M.C. Brupbacher, W.M. Buchta, “Nanostructured thermal spray coatings,” U.S. Provisional Patent Application No. 62/425,213.